Title: Synchronous timing of abrupt climate changes during the last glacial period

Authors: Ellen C. Corrick[1,2*], Russell N. Drysdale[1,2], John C. Hellstrom[3], Emilie Capron[4,5], Sune Olander Rasmussen[5], Xu Zhang[6,7], Dominik Fleitmann[8], Isabelle Couchoud[2,1], Eric Wolff[9]

Affiliations:

[1]School of Geography, The University of Melbourne, Melbourne, Victoria, Australia

[2]EDYTEM, CNRS, Université Savoie Mont Blanc, Université Grenoble Alpes, Chambéry, France

[3]School of Earth Science, The University of Melbourne, Melbourne, Victoria, Australia

[4]British Antarctic Survey, Cambridge, United Kingdom

[5]Physics of Ice, Climate and Earth, Niels Bohr Institute, University of Copenhagen, Copenhagen, Denmark

[6]Key Laboratory of Western China's Environmental Systems (Ministry of Education), College of Earth and Environmental Sciences, Lanzhou University, Lanzhou, 730000, China

[7]Alfred Wegener Institute, Helmholtz Centre for Polar and Marine Research, D-27570 Bremerhaven, Germany

[8]Department of Earth Sciences, University of Basel, 4056 Basel, Switzerland

[9]Department of Earth Sciences, University of Cambridge, Cambridge, United Kingdom

*Correspondence to: ecorrick@student.unimelb.edu.au

Abstract:

Abrupt climate changes during the last glacial period have been detected in a global array of palaeoclimate records but our understanding of their absolute timing and regional synchrony is incomplete. Our compilation of 63 published, independently dated speleothem records shows that abrupt warmings in Greenland were associated with synchronous climate changes across the Asian Monsoon, South American Monsoon and European-Mediterranean regions that occurred within decades. Together with the demonstration of bipolar synchrony in atmospheric response, this provides independent evidence of synchronous high-latitude to tropical coupling of climate changes during these abrupt warmings. Our results provide a globally coherent framework with

which to validate model simulations of abrupt climate change and to constrain ice-core chronologies.

One Sentence Summary: Compilation of 63 speleothem records demonstrates widespread synchronous timing of the onset of interstadials during the last glacial.

Main text

Climate records from Greenland ice cores spanning the last glacial cycle (115,000 – 11,700 years ago) reveal a series of centennial-to-millennial-scale cold-warm oscillations called Dansgaard-Oeschger (DO) events (*1-3*). In Greenland, each event commenced with a rapid transition to warm conditions (a 'Greenland Interstadial', GI) followed by a gradual, then abrupt, return to a cold climate state (a 'Greenland Stadial', GS) (*2*, *3*). This pattern is widely accepted to be associated with changes in the strength of the Atlantic Meridional Overturning Circulation (AMOC), which regulates interhemispheric oceanic heat flux, as captured in the thermal oceanic bipolar seesaw theory (*4-7*). During the DO warm phase, a strong AMOC exports heat from the south and tropics to the high latitudes of the North Atlantic, leading to cooling of the global ocean north of the Antarctic Circumpolar Current (ACC) and reduced temperatures over Antarctica (*6*). At times of DO cooling, a weakened AMOC reduces northward ocean heat transport and results in heat accumulation in the Southern Ocean, leading to Antarctic warming. These changes are broadly reflected in ocean-sediment records across the Atlantic (*8-10*) as far south as the mid-latitude South Atlantic, where both surface (*4*) and deep-ocean signals (*11*) show a similar abruptness and timing to those seen in the North Atlantic, but of opposite sign in surface ocean temperature. Further poleward, the abruptness is dampened by the ACC, which influences heat flux into and out of the

Southern Ocean (*4-6*). This ultimately leads to less abrupt air-temperature changes over Antarctica (*12*), whose onsets lag the Greenland counterparts by around 200 ± 100 years (*13*). The Antarctic changes are therefore symptomatic of a slow-oceanic response to the abrupt changes recorded north of the ACC *(6, 15)*.

Changes to the cross-hemisphere ocean-temperature difference induced by switches in AMOC mode drive meridional shifts in the atmospheric mean state, particularly the position of the Intertropical Convergence Zone (ITCZ) (*14*, *15*). This is most vividly observed in terrestrial monsoon records from both sides of the equator (*16*, *17*) at times when Greenland climate switches abruptly from a stadial to an interstadial (termed here an 'interstadial onset'), and is supported by numerical climate model outputs (*18-20*) (Fig. 1). These higher-amplitude warming episodes correspond to air-temperature increases over the Greenland ice sheet of up to 16°C (*21*), typically in around 80 years. Such a strong high-latitude-to-tropical teleconnection indicates widespread atmospheric reorganisation at the onset of interstadials. However, there is uncertainty over the exact phasing: were climate responses synchronous between different monsoon regions, and between the wider tropical realm and Greenland? Recent reassessments of ice-core data (*22*, *23*) suggest that atmospheric changes associated with abrupt warming and cooling in Greenland were transmitted more or less synchronously as far south as the Antarctic ice sheet, indicating rapid reorganisation of atmospheric circulation. Such bipolar synchrony implies that mid-latitude and tropical regions also responded rapidly as Greenland temperatures changed abruptly. This has been the assumption in previous studies (e.g. (*24*, *25*)), but has yet to be rigorously tested. Answering these questions will deepen our understanding of the underlying dynamics of global climate

teleconnections during abrupt climate changes, which serves as a basis to test climate models used for future projections (*26*).

Testing the large-scale synchrony of stadial-interstadial changes to augment the suggestion of bipolar synchrony is hampered by the limited availability of independently dated palaeoclimate time series with sufficiently constrained chronologies (2σ age uncertainties in the range of decades to centuries). Indeed, the chronologies of many last-glacial records are simply aligned to other marine, ice-core or speleothem age models under the assumption that abrupt events did occur synchronously between sites at the resolution of the records in question *(25, 27, 28)*. This prevents any independent assessments of potential regional leads and lags between these records *(29)*. The current Greenland Ice Core Chronologies (GICC05 and its extension GICC05modelext) *(30-32)* provide the chronological framework for the latest event stratigraphy of abrupt climate changes *(3)*, but published age uncertainties in the annual-layer counting accumulate with increasing age, reaching ± 2,600 years at 60 kyr before 1950 (BP). Beyond this, age uncertainties of the flow-model extension to the chronology, GICC05modelext, are unquantified *(32)*. Thus, any comparison of the timing of interstadials and stadials between ice cores and other archives becomes less certain through time, even though the incremental nature of the ice-core counting errors produces high-precision constraints on the time difference between successive events, i.e. duration of and spacing between events (Fig. S1).

Speleothem records of interstadial onset

To test the global synchrony of these events we investigated the timing of the abrupt interstadial onset for 25 major and 28 minor interstadial events (*3*, *33*) using 63 published, high-resolution and

precisely dated speleothem records covering the last glacial period (Fig. 1; *(34)*; Table S1). Speleothems (secondary mineral deposits found in caves) have great potential because they can be radiometrically dated with great accuracy by uranium-series methods to a precision of 0.1 – 1% (2σ) over last-glacial timescales (e.g. *(35)*). Numerous speleothem oxygen-isotope ($\delta^{18}O$) records spanning the Northern Hemisphere (NH) mid-latitudes to the Southern Hemisphere (SH) sub-tropics capture stadial-interstadial transitions, particularly the more pronounced interstadial onsets, where local precipitation and/or temperature changes lead to significant changes in $\delta^{18}O$ *(17, 36, 37)*.

We standardised all speleothem time-series to avoid methodological bias in age calculations and depth-age model construction, then identified the onset of each interstadial by adapting a technique applied to the ice-core record *(3)* (*(34)*; Fig. S2). Due to the nature of speleothem growth, variability is exhibited in the temporal span of each record, with the majority covering a few tens of thousands of years, although some are much shorter (Fig. S3). Within a single record the temporal resolution may vary greatly, due to changes in the growth rate of the speleothem. All records are dated directly using uranium-thorium methods, and each time series is free of synchronisation to any tuning target. The isotope records for all speleothems are presented in Data S3. Of the 53 interstadials identified in the ice cores *(3)*, 39 could be confidently resolved in at least two records in the speleothem dataset, with the overwhelming majority of records falling into either the Asian Summer Monsoon (ASM), the South American Monsoon (SAM), or the Europe-Mediterranean (EM) domains *(34)* (Fig. 1). The speleothem $\delta^{18}O$ in these three regions exhibits well-documented changes across interstadial onsets (Fig. 2), with patterns generally well reproduced in DO-type transient climate-model simulations (see background maps in Fig. 1). In

the ASM domain, warming in the North Atlantic is associated with a strengthening of both the Indian and East Asian Summer Monsoon subsystems, which produces decreased $\delta^{18}O$ values driven by variations in rainout, air-mass trajectories and/or rainfall amounts *(36-38)* (Fig. 1a). The $\delta^{18}O$ in the SAM domain increases due to the same processes under a weakened monsoon *(39)* (Fig. 1b). This 'monsoon-seesaw pattern' over interstadial onsets is consistent with a northward shift of the ITCZ (*10*, *17*). In the EM region, the speleothem $\delta^{18}O$ response to interstadial onsets is slightly more complex. Sites situated around the Alps and western Turkey (i.e. Sofular) show increased isotopic values *(40, 41)* as the climate warms, consistent with the dominating temperature effect (Fig. 1c) on the $\delta^{18}O$ of local precipitation *(42)*, whilst seasonal changes in moisture source and the source effect cause $\delta^{18}O$ values in north-eastern Turkey (i.e. Karaca) to decrease *(43)*. Around the Mediterranean, regional warming increases the amount of rainfall reaching cave sites *(44)*, leading to decreasing $\delta^{18}O$ values due to the rainfall amount effect *(42)*. This effect also occurs in the eastern Mediterranean where it may be modified by changes in local sea-water $\delta^{18}O$ composition related to higher Nile discharge *(45)*. The abruptness of speleothem $\delta^{18}O$ change at the onset of the interstadials (Fig. 2) is, in most cases, comparable to what is observed in the ice-core record (e.g. *(41)*), when accounting for differences in temporal resolution, speleothem age-model uncertainties and the smoothing of atmospheric signals in speleothems due to groundwater transport and mixing processes in the karst aquifer *(46)*.

Testing the synchrony of interstadial onset

In restricting our comparison to the three regions best represented by the speleothem data, we first tested the intra-regional synchrony of an interstadial onset, hypothesising that abrupt changes *within* a single region should be recorded practically simultaneously by speleothems at each cave

site. Second, we tested the synchrony *between* the three regions for each interstadial onset. The degree of intra- and inter-regional synchrony was assessed using the reduced chi-square statistic, known in geochronology as the mean-square weighted deviation (MSWD) *(47, 48)*, which tests if a group of radiometric ages belong to a single population *(34)*. Where we found statistical agreement between speleothem ages from the same region, we calculated the error-weighted mean (EWM) *(34)* and assigned this as the 'regional age'. These regional ages were used to test the synchrony between regions and to derive a composite speleothem age for each interstadial onset in cases where data from multiple regions were available. These age estimates for interstadial onsets form the Speleothem Interstadial Onset Compilation data set (SIOC19). We also assessed the extent to which an age estimate for the timing of an interstadial onset based on data from only one region could be used as a wider event-age indicator. We then compared the SIOC19 age estimates for each interstadial onset with their timing in the ice-core GICC05 and GICC05modelext chronologies *(3)*. Finally, we investigated the regional age offset over events for which two or more speleothem records from the same region were available.

For 34 of the 37 interstadials recorded in multiple speleothem records, there is strong intra-regional agreement (within 2σ uncertainties), comprising cases where one (n=9) or multiple (n=25) regions are represented (Fig. 2; Table S2; Fig. S4). The three remaining onsets (into interstadials 12a, 14e and 23.1) show disagreement within all of the represented regions (i.e. the MSWD lies outside the accepted range; *(34)*) and we assigned an indeterminate result to these (Table. S2d). Three of the 34 transitions show disagreement within one or more of the regions represented (interstadials 4 – ASM and EM, 12c - ASM, 24.2 – ASM), so we excluded the data from the anomalous region from further (inter-regional) comparisons (region listed as 'unresolved' in Table S2a-b). The strong

overall intra-regional agreement validates the assumption of intra-regional synchrony. This enables us to treat the records from each region as a single population and combine them into a single regional age, based on the EWM, with a reduced uncertainty relative to the individual records. It is likely that significant age differences within a region may be due to either sample and/or site-specific processes affecting the registration of the climate signal (e.g. competing mechanisms driving local $\delta^{18}O$) or chronological issues such as undetected growth hiatuses, uranium leaching *(49)* and/or sub-optimal positioning of uranium-thorium age or stable isotope samples.

In comparing the regional EWM ages, we find strong evidence of synchronous onset for 23 of the 25 interstadials for which we were able to make inter-regional comparisons (Table 1, dark blue shading, Fig. 2, Table S2, Fig. S4). In the case of onsets younger than 40 kyr BP, the difference in the mean age between any region represented by multiple speleothem records (thus giving greater confidence and narrowing the regional uncertainty) ranges from 3 to 72 years (Table S2), with an uncertainty that spans zero. This indicates that the onset of interstadials is likely synchronous within decades. It also highlights that the major limiting factor in deriving more precise constraints of event synchrony is related to the magnitude of the uranium-thorium dating errors of individual speleothem records, rather than scatter in the ages themselves.

The onset of the two interstadials that are not recorded synchronously between regions are those to interstadial 15.1 (recorded 334 ± 185 years earlier in the EM compared to the ASM) and interstadial 23.2 (recorded 716 ± 287 years later in the EM compared to the ASM); in both cases, there were no high-quality records from the SAM region (Fig. 2B, Table S2c). These anomalies

could reflect a genuine asynchrony, implying that these interstadials are of an unusual nature in the context of the other 23. However, such asynchrony may reflect varying sensitivity to these short-lived interstadials, also suggested by some structural difference to the very sharp peaks in Greenland. The regional lead-lag is not consistent however, so does not suggest a systematic regionally asynchronous response to interstadials of this type.

Given that the great majority of interstadial onsets tested for inter-regional synchrony (23 out of 25) show chronological agreement, it is reasonable to assume that an EWM age estimate for an event where only a single region is represented (n = 9: Table 1, light-blue shading; Table S2b) is also indicative of a transition's broader timing. We tested this assumption by comparing the spacing of consecutive interstadial onsets in the speleothems with the corresponding annual-layer-counted intervals in the GICC05 ice-core record *(3, 31, 50)* (Fig. 3). As noted earlier, whilst the precision on the absolute ages of the GICC05 chronology decreases significantly back in time, the interval between the onset of consecutive interstadials over the layer-counted section (0 – 60 kyr BP) can be estimated with relatively high precision (5.7 ± 1.5%, 1σ) (Fig. 3; Fig. S1). Interstadial duration estimates based on the SIOC19 age estimates (including those based on data from only one region) agree within uncertainty with those from the GICC05 chronology, with the exception of one interval out of 22 (interval 12c – 11, GICC05 estimate 3.52 ± 0.18 kyr, SIOC19 3.89 ± 0.16 kyr) (Fig. 3). Beyond the layer-counted section (>60 kyr BP), only two out of nine intervals show discrepancies outside of the uncertainty estimate of SIOC19 (interval 19.2 – 18, GICC05modelext 8.240 kyr, SIOC19 6.998 ± 0.312 kyr; interval GI-18 - 17.2 GICC05modelext 4.660 kyr, SIOC19 5.107 ± 0.273 kyr) (Fig. 3). Overall, however, the agreement between SIOC19 and the GICC05 and GICC05modelext chronologies for the duration of consecutive interstadials validates the

accuracy of the relative ages (within uncertainties) of the single-region estimates, and thus their inclusion alongside the multi-regional EWM ages. Nevertheless, we suggest that the timing estimates of interstadial onsets based on data from only a single region should be treated cautiously until they are verified by additional high-quality speleothem records from other regions.

The fact that the regional speleothem ages of interstadial onsets from three geographically diverse areas are likely synchronous well within a century suggests that the timing should agree – within the same uncertainty – with corresponding events in Greenland. We now evaluate the GICC05 and GICC05modelext chronologies by comparing speleothem and ice-core ages for the 32 interstadials in Table 1. The multi-region (n=23) and single-region (n=9) speleothem age estimates are all within 1.1% of the ice-core mean ages (Table 1; Fig. S6 A). Three of the four largest offsets (20c, 19.2, 18) are observed beyond the layer-counted interval, where ice-core chronological control is less secure due to uncertainties associated with the glaciological modelling that underpins this section (GICC05modelext) (*32*). We do not detect any systematic GICC05-to-SIOC19 age difference that could be linked to either background climate state, or interstadial duration, amplitude and rate of warming (Fig. S6 C-F).

Since the interstadial onsets captured by the speleothems are sufficient in number and encompass the entire range of interstadial types for the last glacial (e.g. including longer-duration events and rebound-type events), they can therefore be regarded as a representative sample of the population of *all* last glacial interstadial onsets. Based on this assumption, we quantified the GICC05-to-SIOC19 age difference across all 23 events younger than 60 ka using robust regression (GICC05 versus SIOC19 ages; *(34)*). The regression yields a slope of 1.000 and a *y*-intercept (i.e. mean age

difference) of -48 (-160/+240) years (Fig. S6 B), providing compelling evidence that the speleothem and ice-core ages agree to within, at a maximum, a couple of centuries. These radiometric-age comparisons provide strong support for the accuracy of both the GICC05 and GICC05modelext chronologies throughout the duration last glacial period, and suggest that the quoted uncertainties are too conservative. Based on our time points for the time period, we do not find strong support for GICC05 being too young over the period 45 – 15 kyr BP as is suggested by linking the GICC05 and U-Th timescales through the use of cosmogenic radionuclides *(51)*, nor can we confirm the 0.63% counting bias correction found by correlation to Hulu cave U-Th dates during the dating of the WAIS Divide ice core *(24)*. Such differences may arise due to methodological approach, including the choice of detrital-thorium correction and depth-age modelling (see *(34)*). The effect of compiling multiple speleothem records is also likely to be significant, in that the influence of potentially younger or older individual records is not as dominant. Our study also looks across the whole of the last glacial period, rather than subsections or the individual temporal span of selected records.

Whilst overall synchrony between individual monsoon regions, and between Europe and the monsoon regions, has been assumed (e.g. *(25, 41)*) it has yet to be fully tested quantitatively. To examine this further, we undertook two steps. First, we computed the EWM (and 95% uncertainties) of the differences between the Asian and South American Monsoon speleothem age estimates for each interstadial onset, where a zero mean would indicate perfect synchrony (Table S3 A). We included only the interstadial onsets in which both monsoon regions were represented by two or more speleothem records (n=8) on the grounds that multiple speleothem records for an onset provide a more robust age estimate. The results give an EWM age difference (ASM minus

SAM) of 19 ± 113 years (MSWD = 0.26) (blue PDF curve in Fig. 4A; Table S3A). This strong degree of synchrony suggests the ASM and SAM regions can be treated as a single category to yield 'monsoon' EWM ages (and 95% uncertainties). Second, we then determined the age difference between the EM and combined monsoon regions for the same onsets. There are six interstadials (3, 8c, 9, 10, 12c and 13c) for which there are at least two records from the EM region *and* at least two monsoon records (regardless of their origin). The mean onset-age difference and uncertainty (EM minus Monsoon) is 25 ± 84 years (MSWD = 0.90) (red PDF curve in Fig. 4A; Table S3B). This implies that the 95th percentile EM lead and EM lag over the monsoon regions is 109 years and 59 years respectively.

Comparison with model output and implications

We now compare the regional phasing of the onset of interstadials as indicated by the speleothems with modelling simulations and previous research (*12*, *14*, *23*, *24*) to attain an overall picture regarding global climate teleconnection during an abrupt interstadial onset associated with AMOC recovery. We employed long-term North Atlantic hosing experiments *(52)*, in which a ~0.2 Sv freshwater flux was released to the Ruddiman Belt for 1000 years to mimic a cold 'stadial' climate state. As the freshwater flux is removed at the 501st model year (1st model year in Fig. 4), the AMOC starts increasing instantly and reaches its 'interstadial' state within a century (Fig. 4). We acknowledge that other forcing factors (e.g. ice-sheet height and atmospheric CO_2) are also able to mimic DO-type abrupt AMOC changes (*19*, *20*), and freshwater flux may not be a realistic forcing factor for all interstadials (i.e. non-Heinrich stadials). However, freshwater forcing is the ideal surrogate to evaluate the role of AMOC changes on the spatial phasing of climate changes

(53), since changes in ice-sheet height and atmospheric CO_2 will exert additional regional and global climate responses that are not associated with AMOC changes *(19, 20)* (*(34)*; Fig. S7).

The climate response to AMOC reinvigoration expressed in the modelled regional climate anomalies is consistent with the observations from the regional array of speleothems (Fig. 4). Furthermore, the degree of synchrony shown by the speleothems between ASM and SAM, and EM and the combined Monsoon, agrees with the timing of modelled regional precipitation and temperature anomalies in the Monsoon and EM respectively (Fig. 4). Based on this we can summarise the pattern of climate changes during the interstadial onsets in three stages (Fig. 4 B-K). At the beginning, AMOC recovery (Fig. 4B) will lead to an initial warming anomaly in the northern North Atlantic (Fig. 4C-D), causing thermal asymmetry between the North and South Atlantic. This would drive a fast atmospheric response in which the Atlantic ITCZ starts migrating towards the subtropical North Atlantic (Fig. 4 yellow shading). As the AMOC is strengthened further, the entire NH warms, pulling the ITCZ further northwards globally (Fig. 4 E-H, pink shading). This strengthening (weakening) of the ASM (SAM) leads to the observed decrease (increase) in speleothem $\delta^{18}O$ records *(37-39)*. Over Europe and the Mediterranean, warming drives increased speleothem $\delta^{18}O$ at sites where the local rainfall $\delta^{18}O$ is most sensitive to mean atmospheric temperature changes *(40, 41)* and lower speleothem $\delta^{18}O$ at sites where warmer ocean temperatures drive higher rainfall amounts *(44)*. Meanwhile, Antarctica starts perceiving the northern signal via the atmospheric bridge *(6, 22)*. This is evident in the model output of changes to the Southern Annular Mode index, a proxy for meridional changes in the position of the westerlies: as interstadial onset commences, and the ITCZ shifts northward, the index becomes more negative over a similar time frame to the ITCZ changes (Fig. 4 I). This is consistent with a

northward migration of the southern mid-latitude westerlies and supports the conceptual model proposed by ref. *(23)* to explain the changes in the *d*-excess of Antarctic ice across the warming transitions. Once the AMOC reaches interstadial mode (Fig. 4 blue shading), atmospheric circulation assumes its interstadial mean state, leading to a cascade of processes that alters heat transport across the ACC, leading to an Antarctic temperature decrease *(6)* (Fig. 4 K) that lags the AMOC recovery (and Greenland warming: Fig. 4 C) by approximately 200 ± 100 years *(13)* (Fig. 4A brown pdf). The compilation of precise speleothem records now lends support to this pattern of changes and provides crucial empirical evidence for the synchronous response to these changes in the mid-latitudes.

The SIOC19 age estimates (Table 1) constitute the most precise, absolute dating of interstadial onsets yet produced. Using the full range of interstadial types across the whole last glacial period, and incorporating as much speleothem information as possible from the target regions, we demonstrate that synchronous climate changes (within a century) occurred between Europe and the Asian and South American monsoon domains at the onset of interstadials. A similar level of synchrony is observed between Europe and both monsoon regions (Fig. 4 A). Given the proximity of Greenland to EM, compared to the proximity of the EM to both monsoon domains, it is highly likely that such synchrony extends across the North Atlantic to Greenland. A recent comparison, based on four speleothem records, of interstadials in the latter part of the last glacial (<45 kyr BP) also shows the timing of the onset to be synchronous within uncertainties *(51)*. Our findings are also consistent with a previous study of a single interstadial, where synchrony between tropical (using methane as a proxy) and Greenland temperatures took place within 24 years *(54)*. Thus, our study strongly supports the long-held, but theretofore untested, assertions of practically

synchronous high-latitude-to-tropical climate changes during abrupt interstadial onsets *(24, 25, 28)*. Recent results from Antarctica suggest that changes in the source location of moisture reaching the ice sheet were abrupt and occurred within decades of DO warmings (and coolings) in Greenland *(22)*, implying an interpolar atmospheric teleconnection. Our results provide crucial, independent supporting evidence of near-synchronous atmospheric propagation of abrupt climate changes during interstadial onsets that were global in scale by providing spatial detail between the NH mid-latitudes and the SH subtropics.

The prospect of future abrupt climate change under global warming, and the importance of reliable climate-model predictions, has brought past abrupt changes, such as DO events, into sharp focus in recent years. Our study provides precise chronological information on the timing of climate changes during stadial-interstadial transitions, reveals the widespread synchrony of their response and provides radiometric validation and constraint for refining ice-core chronologies. The triggering mechanism for DO events (and the associated AMOC changes), however, remains an open question, and discriminating between external forcing (e.g. ice-sheet height, greenhouse gases, meltwater, volcanism) *(18, 19, 55, 56)* and "self-oscillation" mechanisms *(57)* as drivers of AMOC-mode transitions rests with future studies that take advantage of state-of-the-art Earth-system models and well-dated, high-resolution palaeoclimate records.

Fig. 1. Location of last glacial speleothem records included in the compilation. Cave sites for records from the Asian Summer Monsoon region (A), South American Monsoon region (B) and Europe-Mediterranean region (C). Grey triangles and italicised font represent records that were used in the comparison but are not represented in the age estimates for the synchronous events shown in Table 1. For reference to the numbering see Table S1 which shows the complete list of speleothem records and associated references. Shaded backgrounds are composite anomalies of annual mean precipitation (A and B) and air temperature (C) between interstadial and stadial states in DO-type transient experiments *(19, 20, 34, 52)*.

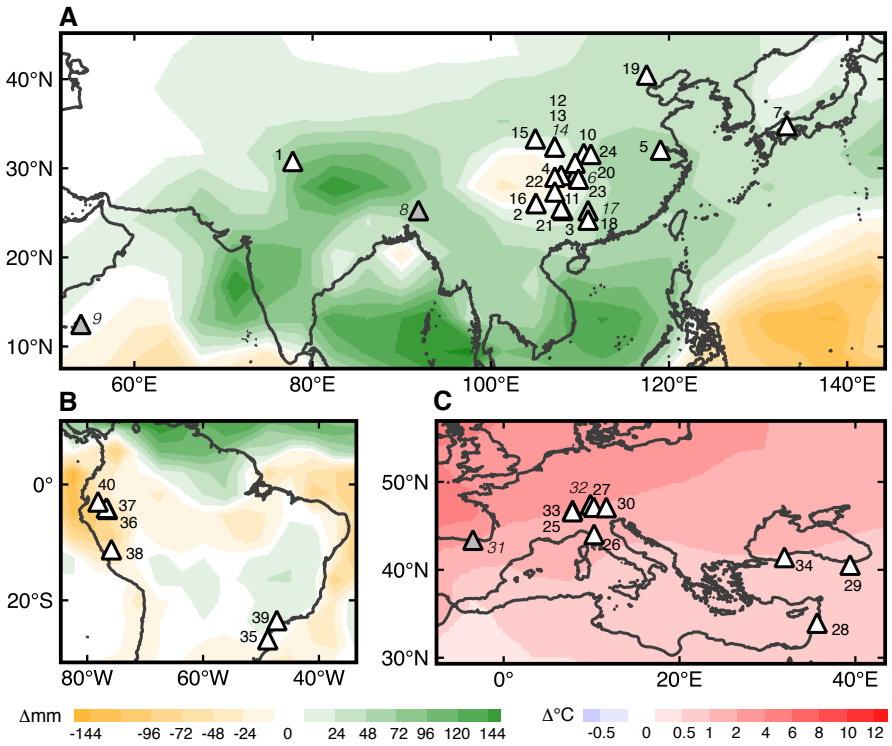
A
40°N
30°N
20°N
10°N
60°E
80°E
100°E
120°E
140°E
B
0°
20°S
80°W
60°W
40°W
C
50°N
40°N
30°N
0°
20°E
40°E
Δmm
-144 -96 -72 -48 -24 0 24 48 72 96 120 144
Δ°C
-0.5 0 0.5 1 2 4 6 8 10 12

Table 1. The timing of each interstadial onset in the combined speleothem records (SIOC19) and the corresponding ages in the Greenland ice-core record. The combined speleothem age is the error-weighted mean (and the corresponding 2σ uncertainty) of multiple individual speleothem records that have been grouped at a regional level (Asian Summer Monsoon, South American Monsoon and Europe-Mediterranean regions). Each event is colour-coded according to the number of regions represented by the corresponding speleothem records: dark blue is all three regions, blue is two of the three regions and light blue is one region; 'n' denotes the total number of speleothem records. The corresponding GICC05 age *(3)* is shown, including the maximum counting error for the annual-layer-counted section (back to 60 kyr BP). No errors are shown beyond 60 kyr BP as the uncertainty on this section of the chronology is not quantified. The age difference between the ice-core and composite speleothem ages is given as both a percentage and absolute difference. Note that the ages in GICC05 are given to the nearest decade based on the 20-year resolution of the data. All ages are reported in years BP (before 1950).

Interstadial number	Combined Speleothem SIOC19	n	GICC05 Age (yrs BP)	% age difference	age difference (yrs)
1e	14,646 ± 34	9	14,642 ± 186	-0.03	-4
3	27,822 ± 72	10	27,730 ± 832	-0.33	-92
4	29,117 ± 189	4	28,850 ± 898	-0.93	-267
5.1	30,980 ± 103	7	30,790 ± 1,024	-0.62	-190
5.2	32,477 ± 115	7	32,450 ± 1,132	-0.08	-27
6	33,699 ± 174	5	33,690 ± 1,212	-0.03	-9
7a	34,884 ± 130	3	34,830 ± 1,293	-0.16	-54
7c	35,342 ± 90	6	35,430 ± 1,321	0.25	88
8c	38,044 ± 88	11	38,170 ± 1,449	0.33	126
9	40,251 ± 81	6	40,110 ± 1,580	-0.35	-141
10	41,431 ± 119	10	41,410 ± 1,633	-0.05	-21
11	43,185 ± 64	7	43,290 ± 1,736	0.24	105
12c	47,071 ± 145	6	46,810 ± 1,912	-0.56	-261
13a	49,015 ± 154	5	49,010 ± 2,021	-0.01	-5
13c	49,439 ± 106	7	49,230 ± 2,031	-0.43	-209
14c	53,713 ± 124	6	53,910 ± 2,289	0.37	197
15.2	55,770 ± 98	5	55,750 ± 2,368	-0.04	-20
16.1a	57,746 ± 311	2	57,870 ± 2,492	0.21	124
16.1c	57,910 ± 293	2	57,990 ± 2,497	0.14	80
16.2	58,315 ± 288	2	58,230 ± 2,511	-0.15	-85
17.1a	58,870 ± 346	2	58,730 ± 2,540	-0.24	-140
17.1c	59,199 ± 241	4	59,030 ± 2,557	-0.29	-169
17.2	59,489 ± 173	6	59,390 ± 2,569	-0.17	-99
18	64,596 ± 211	6	64,050	-0.85	-546
19.2	71,594 ± 230	5	72,290	0.96	696
20c	75,583 ± 248	7	76,390	1.06	807
21.1e	84,621 ± 971	3	84,710	0.11	89
22g	90,386 ± 617	2	89,990	-0.44	-396
24.1a	106,328 ± 325	2	106,170	-0.15	-158
24.1c	106,918 ± 204	3	106,700	-0.20	-218
24.2	108,254 ± 235	2	108,230	-0.02	-24
25c	115,310 ± 209	2	115,320	0.01	10

Fig. 2. Stable isotope records of individual speleothems for each interstadial onset. Each speleothem record displayed has met screening and event identification criteria *(34)* and is color coded according to region (EM = orange, ASM = blue, SAM = purple). All records are plotted on the re-calculated chronology *(34)*. Plots are provided for interstadial onsets found to be synchronous (A) and non-synchronous (B). The NGRIP $\delta^{18}O$ series on the GICC05 or GICC05modelext chronology is plotted in black, with each event position *(3)*, represented by a red square. The corresponding event position in each speleothem record is indicated by a solid black circle (see Data S1 for the timing and uncertainty). Markers with error bars at the top of each panel indicate the age and 2σ uncertainty of the inter-regional age estimate (brown), and intra-regional age estimates (EM = orange, ASM = blue, SAM = purple). Lettering provides the name of each speleothem record. Refer to Table S1 for the full details and reference of each record.

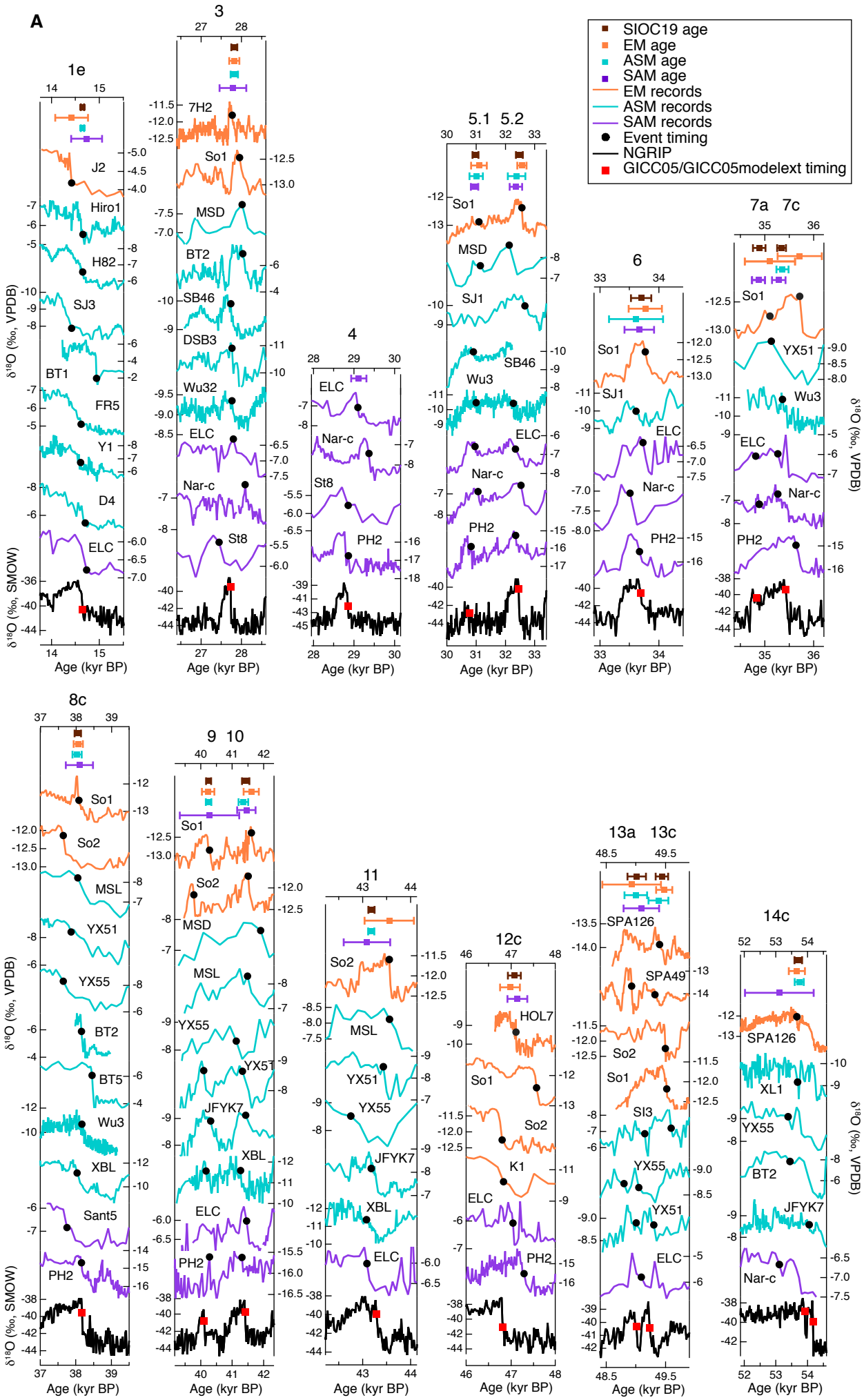
A
SIOC19 age
EM age
ASM age
SAM age
EM records
ASM records
SAM records
Event timing
NGRIP
GICC05/GICC05modelext timing
1e
3
4
5.1 5.2
6
7a 7c
8c
9 10
11
12c
13a 13c
14c
J2
Hiro1
H82
SJ3
BT1
FR5
Y1
D4
ELC
7H2
So1
MSD
BT2
SB46
DSB3
Wu32
Nar-c
St8
PH2
SJ1
Wu3
So2
MSL
YX51
YX55
BT5
XBL
Sant5
JFYK7
HOL7
K1
SPA126
SPA49
SI3
XL1
δ18O (‰, VPDB)
δ18O (‰, SMOW)
Age (kyr BP)

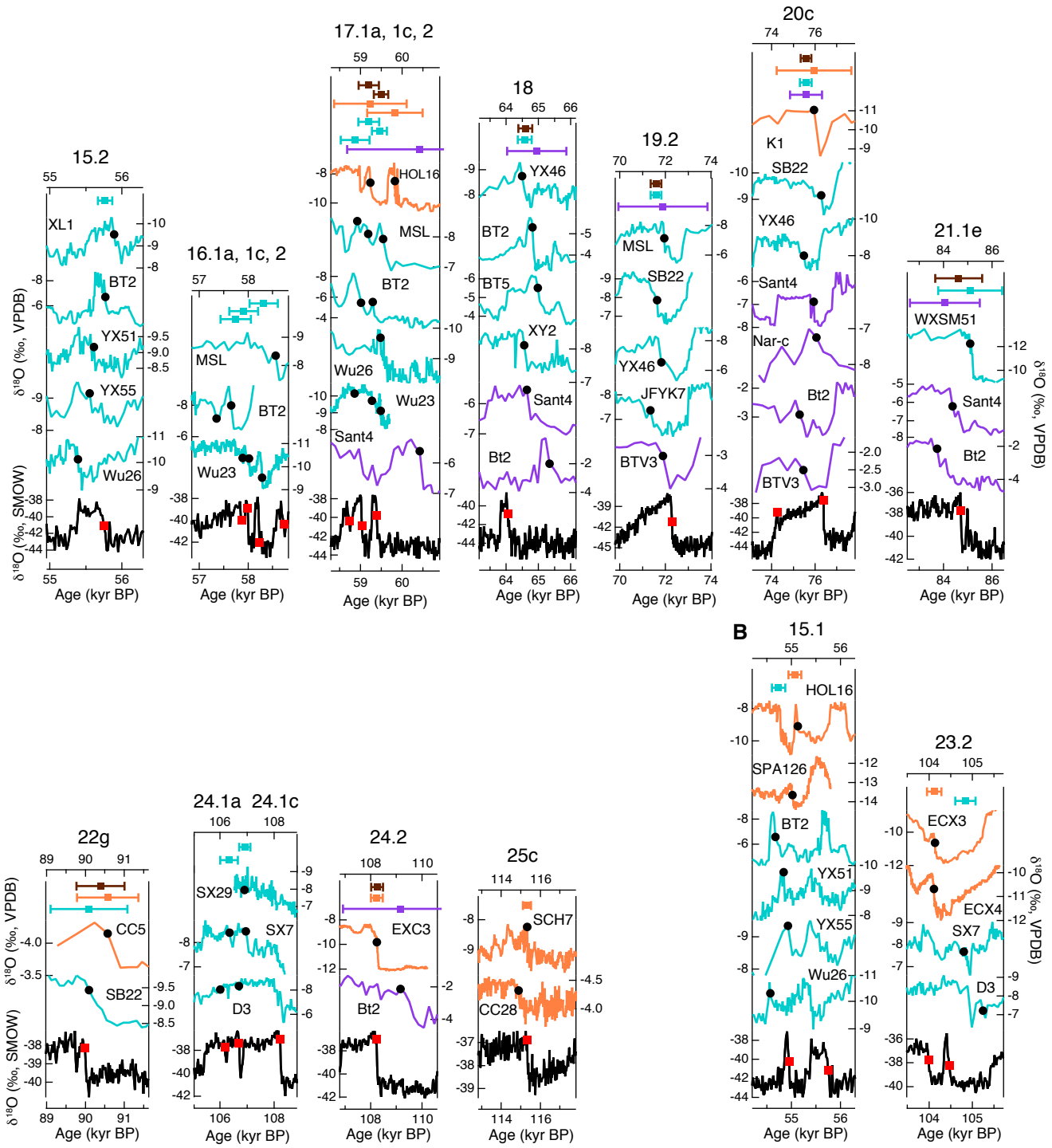
15.2
XL1
BT2
YX51
YX55
Wu26
16.1a, 1c, 2
MSL
BT2
Wu23
17.1a, 1c, 2
HOL16
MSL
BT2
Wu26
Wu23
Sant4
18
YX46
BT2
BT5
XY2
Sant4
Bt2
19.2
MSL
SB22
YX46
JFYK7
BTV3
20c
K1
SB22
YX46
Sant4
Nar-c
Bt2
BTV3
21.1e
WXSM51
Sant4
Bt2
δ18O (‰, VPDB)
δ18O (‰, SMOW)
Age (kyr BP)
22g
CC5
SB22
24.1a 24.1c
SX29
SX7
D3
24.2
EXC3
Bt2
25c
SCH7
CC28
B
15.1
HOL16
SPA126
BT2
YX51
YX55
Wu26
23.2
ECX3
ECX4
SX7
D3

Fig. 3. **Years between the onset of consecutive interstadials**. The time interval between the onset of consecutive interstadials in the GICC05/GICC05modelext chronology is compared to the corresponding interval based on the SIOC19 ages. Error bars represent the 2σ age uncertainties on the interval. For the GICC05 chronology, this was calculated as the change in the accumulated layer-counting uncertainty between events (see Fig. S1); errors are not shown for events within the GICC05modelext section as they are not quantified *(32)*. For the speleothems, the error bar is the uncertainty of the consecutive SIOC19 age estimates in quadrature. The timing between interstadial onsets is shown for those interstadials demonstrated to be synchronous in the speleothems, including estimates based on data from only one region.

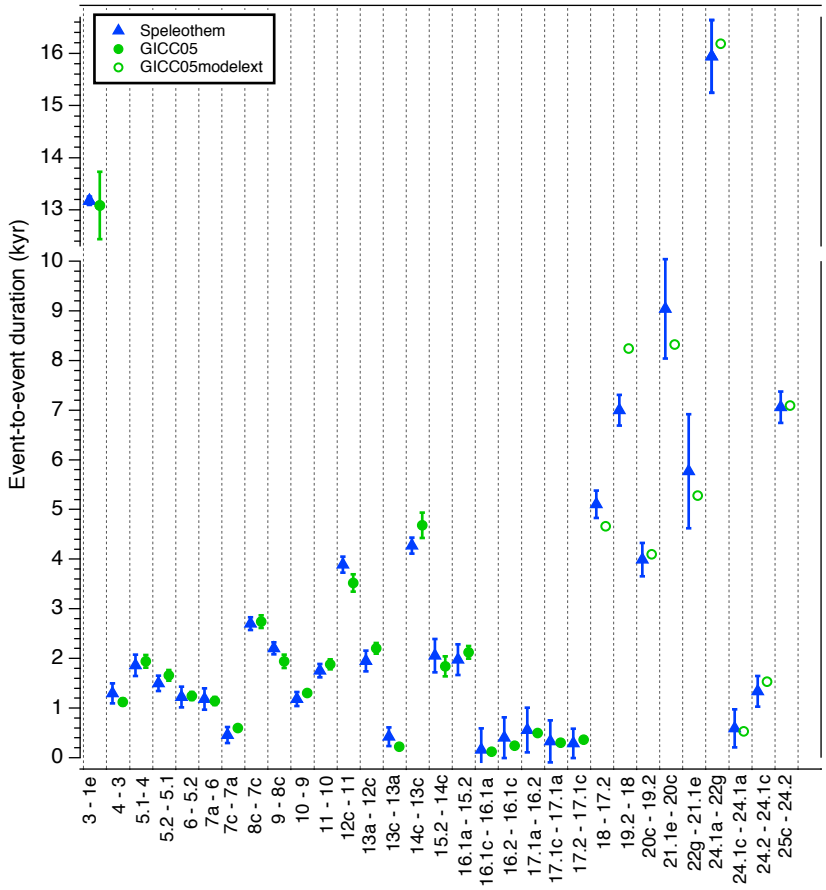
Speleothem
GICC05
GICC05modelext
Event-to-event duration (kyr)
0
1
2
3
4
5
6
7
8
9
10
13
14
15
16
3 - 1e
4 - 3
5.1 - 4
5.2 - 5.1
6 - 5.2
7a - 6
7c - 7a
8c - 7c
9 - 8c
10 - 9
11 - 10
12c - 11
13a - 12c
13c - 13a
14c - 13c
15.2 - 14c
16.1a - 15.2
16.1c - 16.1a
16.2 - 16.1c
17.1a - 16.2
17.1c - 17.1a
17.2 - 17.1c
18 - 17.2
19.2 - 18
20c - 19.2
21.1e - 20c
22g - 21.1e
24.1a - 22g
24.1c - 24.1a
24.2 - 24.1c
25c - 24.2

Fig. 4. Spatial synchrony of climate changes during interstadial onsets. (A) Probability density functions (pdfs) of spatial age offsets between the two monsoon regions (ASM minus SAM, blue) and between Europe and both monsoon regions (EM minus Monsoon, red) based on composite speleothem data (Table S3). Also shown (brown) is the previously determined offset between the West Antarctic Ice Sheet ice core (WAIS) $\delta^{18}O$ and NGRIP $\delta^{18}O$ *(13)*. Lower panel **(B-K)**: simulated climate changes in a DO-type hosing simulation, each expressed as anomalies from the mean of the simulation (see *(34)*, Fig. S6, Table S4). **(B)** AMOC index (defined as maximal meridional stream function at the water-depth of 1500-3000 meters in the North Atlantic); **(C)** annual mean air temperature (MAT) over the NGRIP drilling site; **(D)** annual mean atmospheric temperature (MAT) over the Europe-Mediterranean region (30°N-45°N, 25°E-40°E); mean annual precipitation over the **(E)** Eastern Asian (20°N-30°N, 108°E-120°E), **(F)** Indian (25°N-35°N, 75°E-85°E), and **(G)** South American regions (5°S-10°S, 30°W-75°W); annual mean sea-surface temperature (SST) in **(H)** the tropical-subtropical South Atlantic (5°S-30°S, 60°W-10°E); **(I)** Southern Annular Mode index reflecting changes in sea-level pressure from 20°S-90°S; **(J)** annual mean SST in the Atlantic sector of the Southern Ocean (55°S-75°S, 60°W-10°E); **(K)** MAT over West Antarctica (75°S -82°S, 90°W -135°W) taken to be representative of the WAIS ice core site. Yellow shading represents the period of fast atmospheric response in which the Atlantic ITCZ starts migrating towards the subtropical North Atlantic. Pink shading represents the period of further strengthening of the AMOC and NH warming. Blue shading represents the start of the AMOC interstadial mode. The grey series are raw model outputs and the colour series are 11-year running averages. The black dotted lines are model series derived from the application of a Bayesian, least-squares change-point analysis *(58)* to each raw time series. For all plots **(B-K)** in the lower panel, the *x*-axis shows model years, with year zero reset to the year of the onset of NGRIP warming according to the change-point analysis; for the upper panel **(A)**, the year scale refers to the age offset for each pdf. The NGRIP-WAIS pdf is therefore in its approximate correct position with respect to the model-year scale in the lower panel (see *(34)*).

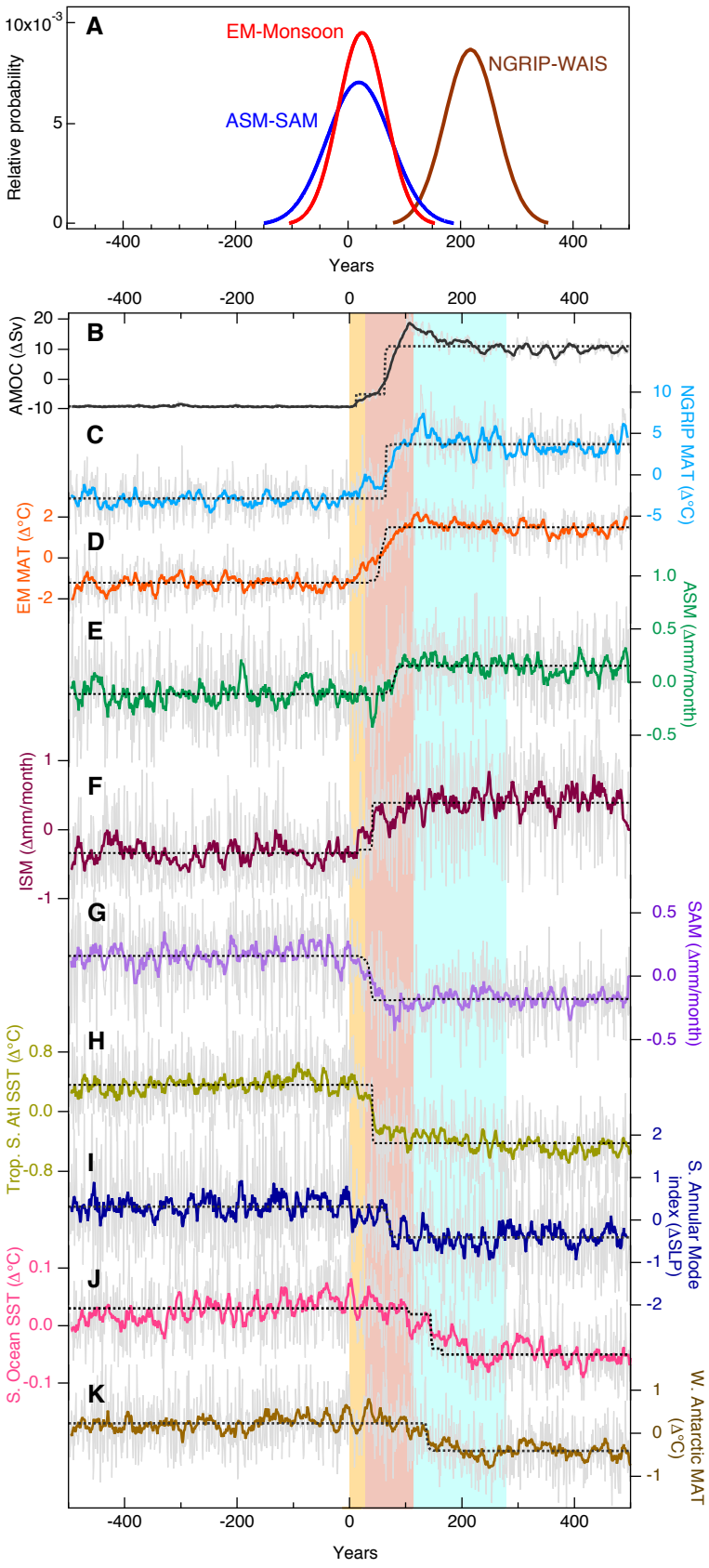
A
EM-Monsoon
NGRIP-WAIS
ASM-SAM
Relative probability
10x10-3
Years
B
C
D
E
F
G
H
I
J
K
AMOC (ΔSv)
NGRIP MAT (Δ°C)
EM MAT (Δ°C)
ASM (Δmm/month)
ISM (Δmm/month)
SAM (Δmm/month)
Trop. S. Atl SST (Δ°C)
S. Annular Mode index (ΔSLP)
S. Ocean SST (Δ°C)
W. Antarctic MAT (Δ°C)
Years

References and notes

1. W. Dansgaard, S. J. Johnsen, H. B. Clausen, D. Dahl-Jensen, N. S. Gundestrup, *et al*., Evidence for general instability of past climate from a 250-kyr ice-core record. *Nature* **364**, 218–220 (1993).

2. NGRIP Members, High-resolution record of Northern Hemisphere climate extending into the last interglacial period. *Nature* **431**, 147–151 (2004).

3. S. O. Rasmussen, M. Bigler, S. P. E. Blockley, T. Blunier, S. L. Buchardt, *et al*., A stratigraphic framework for abrupt climatic changes during the Last Glacial period based on three synchronized Greenland ice-core records: refining and extending the INTIMATE event stratigraphy. *Quaternary Science Reviews* **106**, 14–28 (2014).

4. S. Barker, P. Diz, M. J. Vautravers, J. Pike, G. Knorr, *et al*., Interhemispheric Atlantic seesaw response during the last deglaciation. *Nature* **457**, 1097–1102 (2009).

5. T. F. Stocker, S. J. Johnsen, A minimum thermodynamic model for the bipolar seesaw. *Paleoceanography* **18**, 1087 (2003).

6. J. B. Pedro, M. Jochum, C. Buizert, F. He, S. Barker, *et al*., Beyond the bipolar seesaw: Toward a process understanding of interhemispheric coupling. *Quaternary Science Reviews* **192**, 27–46 (2018).

7. W. S. Broecker, Paleocean circulation during the last deglaciation: A bipolar seesaw? *Paleoceanography* **13**, 119–121 (1998).

8. J. P. Sachs, S. J. Lehman, Subtropical North Atlantic Temperatures 60,000 to 30,000 Years Ago. *Science* **286**, 756–759 (1999).

9. S. Barker, J. Chen, X. Gong, L. Jonkers, G. Knorr, *et al*., Icebergs not the trigger for North Atlantic cold events. *Nature* **520**, 333–336 (2015).

10. L. C. Peterson, G. H. Haug, K. A. Hughen, U. Röhl, Rapid Changes in the Hydrologic Cycle of the Tropical Atlantic During the Last Glacial. *Science* **290**, 1947–1951 (2000).

11. J. Gottschalk, L. C. Skinner, S. Misra, C. Waelbroeck, L. Menviel, *et al*., Abrupt changes in the southern extent of North Atlantic Deep Water during Dansgaard–Oeschger events, *Nature Geoscience* **8**, 950–954 (2015).

12. EPICA Community Members, One-to-one coupling of glacial climate variability in Greenland and Antarctica. *Nature* **444**, 195–198 (2006).

13. C. Buizert, B. Adrian, J. Ahn, M. Albert, R. B. Alley, *et al*., Precise interpolar phasing of abrupt climate change during the last ice age. *Nature* **520**, 661–665 (2015).

14. A. J. Broccoli, K. A. Dahl, R. J. Stouffer, Response of the ITCZ to Northern Hemisphere cooling. *Geophys. Res. Lett.* **33**, L01702 (2006).

15. I. Cvijanovic, P. L. Langen, E. Kaas, P. D. Ditlevsen, Southward Intertropical Convergence Zone Shifts and Implications for an Atmospheric Bipolar Seesaw. *J. Climate* **26**, 4121–4137 (2013).

16. L. C. Kanner, S. J. Burns, H. Cheng, R. L. Edwards, High-Latitude Forcing of the South American Summer Monsoon During the Last Glacial. *Science* **335**, 570–573 (2012).

17. X. Wang, A. S. Auler, R. L. Edwards, H. Cheng, E. Ito, *et al*., Interhemispheric anti-phasing of rainfall during the last glacial period. *Quaternary Science Reviews* **25**, 3391–3403 (2006).

18. A. Ganopolski, S. Rahmstorf, Rapid changes of glacial climate simulated in a coupled climate model. *Nature* **409**, 153–158 (2001).

19. X. Zhang, G. Lohmann, G. Knorr, C. Purcell, Abrupt glacial climate shifts controlled by ice sheet changes. *Nature* **512**, 290–294 (2014).

20. X. Zhang, G. Knorr, G. Lohmann, S. Barker, Abrupt North Atlantic circulation changes in response to gradual CO2 forcing in a glacial climate state. *Nature Geoscience* **10**, 518–523 (2017).

21. C. Lang, M. Leuenberger, J. Schwander, S. J. Johnsen, 16°C Rapid Temperature Variation in Central Greenland 70,000 Years Ago. *Science* **286**, 934–937 (1999).

22. B. R. Markle, E. J. Steig, C. Buizert, S. W. Schoenemann, C. M. Bitz, *et al*., Global atmospheric teleconnections during Dansgaard–Oeschger events. *Nature Geoscience*, 1–7 (2016).

23. C. Buizert, M. Sigl, M. Severi, B. R. Markle, J. J. Wettstein, *et al*., Abrupt ice-age shifts in southern westerly winds and Antarctic climate forced from the north. *Nature*, 1–19 (2018).

24. C. Buizert, K. M. Cuffey, J. P. Severinghaus, D. Baggenstos, T. J. Fudge, *et al*., The WAIS Divide deep ice core WD2014 chronology Part 1: Methane synchronization (68–31 ka BP) and the gas age–ice age difference. *Clim. Past* **11**, 153–173 (2015).

25. K. A. Hughen, J. Southon, S. Lehman, C. Bertrand, J. Turnbull, Marine-derived C-14 calibration and activity record for the past 50,000 years updated from the Cariaco Basin. *Quaternary Science Reviews* **25**, 3216–3227 (2006).

26. G. Flato, J. Marotzkw, B. Abiodun, P. Braconnot, S. C. Chou, *et al*., *Evaluation of Climate Models: Climate Change The Physical Science Basis. Contribution of Working Group I to the Fifth Assessment Report of the Intergovernmental Panel on Climate* T. F. Stocker, D. Qin, G. Plattner, M. Tigor, S. K. Allen, J. Boschung, A. Nauels, Y. Xia, V. Bex, P. M. Midgley, Eds. (Cambridge University Press, 2013).

27. G. Bond, W. S. Broecker, S. J. Johnsen, J. McManus, L. Labeyrie, *et al*., Correlations between climate records from North Atlantic sediments and Greenland ice. *Nature* **365**, 143–147 (1993).

28. N. J. Shackleton, H. Michael, E. Vincent, Phase relationships between millennial-scale events 64,000 -24,000 years ago. *Paleoceanography* **15**, 565–569 (2000).

29. M. Blaauw, Out of tune: the dangers of aligning proxy archives. *Quaternary Science Reviews* **36**, 38–49 (2010).

30. K. K. Andersen, A. Svensson, S. J. Johnsen, S. O. Rasmussen, M. Bigler, *et al*., The Greenland Ice Core Chronology 2005, 15 42 ka. Part 1: constructing the time scale. *Quaternary Science Reviews* **25**, 3246–3257 (2006).

31. A. Svensson, K. K. Andersen, M. Bigler, A 60 000 year Greenland stratigraphic ice core chronology. *Clim. Past* (2008).

32. E. W. Wolff, J. Chappellaz, T. Blunier, S. O. Rasmussen, A. Svensson, Millennial-scale variability during the last glacial: The ice core record. *Quaternary Science Reviews* **29**, 2828–2838 (2010).

33. E. Capron, A. Landais, J. Chappellaz, A. Schilt, D. Buiron, *et al*., Millennial and sub-millennial scale climatic variations recorded in polar ice cores over the last glacial period. *Clim. Past* **6**, 345–365 (2010).

34. *See supplementary material*.

35. W.-H. Duan, H. Cheng, M. Tan, R. L. Edwards, Onset and duration of transitions into Greenland Interstadials 15.2 and 14 in northern China constrained by an annually laminated stalagmite. *Sci Rep* **6**, 20844–6 (2016).

36. H. Cheng, R. L. Edwards, A. Sinha, C. Spötl, L. Yi, *et al*., The Asian monsoon over the past 640,000 years and ice age terminations. *Nature* **534**, 640–646 (2016).

37. G. Kathayat, H. Cheng, A. Sinha, C. Spötl, R. L. Edwards, *et al*., Indian monsoon variability on millennial-orbital timescales. *Sci Rep* **6**, 24374–7 (2016).

38. S. Chen, Y. Wang, H. Cheng, R. L. Edwards, X. Wang, *et al*., Strong coupling of Asian Monsoon and Antarctic climates on sub- orbital timescales. *Sci Rep*, 1–8 (2016).

39. H. Cheng, A. Sinha, F. W. Cruz Jr., X. Wang, R. L. Edwards, *et al*., Climate change patterns in Amazonia and biodiversity. *Nature Communications* **4**, 1411–6 (2013).

40. G. E. Moseley, C. Spotl, A. Svensson, H. Cheng, S. Brandstatter, *et al*., Multi-speleothem record reveals tightly coupled climate between central Europe and Greenland during Marine Isotope Stage 3. *Geol* **42**, 1043–1046 (2014).

41. D. Fleitmann, H. Cheng, S. Badertscher, R. L. Edwards, M. Mudelsee, *et al*., Timing and climatic impact of Greenland interstadials recorded in stalagmites from northern Turkey. *Geophys. Res. Lett.* **36**, L19707–5 (2009).

42. W. Dansgaard, Stable isotopes in precipitation, *Tellus A* **16** (1964), doi:10.3402/tellusa.v16i4.8993.

43. P. J. Rowe, J. E. Mason, J. E. Andrews, A. D. Marca, L. Thomas, *et al*., Speleothem isotopic evidence of winter rainfall variability in northeast Turkey between 77 and 6ka. *Quaternary Science Reviews* **45**, 60–72 (2012).

44. R. N. Drysdale, G. Zanchetta, J. C. Hellstrom, A. E. Fallick, J. McDonald, *et al*., Stalagmite evidence for the precise timing of North Atlantic cold events during the early last glacial. *Geol* **35**, 77–4 (2007).

45. H. Cheng, A. Sinha, S. Verheyden, F. H. Nader, X. L. Li, *et al*., The climate variability in northern Levant over the past 20,000 years. *Geophys. Res. Lett.* **42**, 8641–8650 (2015).

46. E. Hodge, J. McDonald, M. Fischer, D. Redwood, Q. Hua, *et al*., Using the 14C Bomb Pulse to Date Young Speleothems. *Radiocarbon* **53**, 345–357 (2011).

47. I. Wendt, C. Carl, The statistical distribution of the mean square weighted distribution. *Chemical Geology* **86**, 275–285 (1991).

48. P. W. Reiners, R. W. Carlson, P. R. Renne, K. M. Cooper, D. E. Granger, *et al*.. *Geochronology and Thermochronology* (John Wiley and Sons Ltd, 2018).

49. P. Bajo, J. C. Hellstrom, S. Frisia, R. N. Drysdale, J. Black, *et al*., "Cryptic" diagenesis and its implications for speleothem geochronologies. *Quaternary Science Reviews* **148**, 17–28 (2016).

50. A. Svensson, K. K. Andersen, M. Bigler, H. B. Clausen, D. Dahl-Jensen, *et al*., The Greenland Ice Core Chronology 2005, 15–42ka. Part 2: comparison to other records. *Quaternary Science Reviews* **25**, 3258–3267 (2006).

51. F. Adolphi, C. Bronk Ramsey, T. Erhardt, R. L. Edwards, H. Cheng, C. S. M. Turney, *et al*., Connecting the Greenland ice-core and U/Th timescales via cosmogenic radionuclides: testing the synchroneity of Dansgaard–Oeschger events. *Clim. Past* **14**, 1755–1781 (2018).

52. X. Zhang, G. Lohmann, G. Knorr, X. Xu, Different ocean states and transient characteristics in Last Glacial Maximum simulations and implications for deglaciation. *Clim. Past* **9**, 2319–2333 (2013).

53. M. Kageyama, U. Merkel, B. Otto-Bliesner, M. Prange, A. Abe-Ouchi, *et al*., Climatic impacts of fresh water hosing under Last Glacial Maximum conditions: a multi-model study. *Clim. Past* **9**, 935–953 (2013).

54. J. L. Rosen, E. J. Brook, J. P. Severinghaus, T. Blunier, L. E. Mitchell, *et al*., An ice core record of near-synchronous global climate changes at the Bølling transition. *Nature Geoscience* **7**, 459–463 (2014).

55. G. Knorr, G. Lohmann, Southern Ocean origin for the resumption of Atlantic thermohaline circulation during deglaciation. *Nature* **424**, 532–536 (2003).

56. J. U. L. Baldini, R. J. Brown, J. N. McElwaine, Was millennial scale climate change during the Last Glacial triggered by explosive volcanism? *Sci Rep* **5**, 17442–9 (2015).

57. W. R. Peltier, G. Vettoretti, Dansgaard-Oeschger oscillations predicted in a comprehensive model of glacial climate: A "kicked" salt oscillator in the Atlantic. *Geophys. Res. Lett.* **41**, 7306–7313 (2014).

58. E. Ruggieri, A Bayesian approach to detecting change points in climatic records. *Int. J. Climatol.* **33**, 520–528 (2012).

59. H. Cheng, R. L. Edwards, C.-C. Shen, V. J. Polyak, Y. Asmerom, *et al.*, Improvements in 230Th dating, 230Th and 234U half-life values, and U–Th isotopic measurements by multi-collector inductively coupled plasma mass spectrometry. *Earth and Planetary Science Letters* **371-372**, 82–91 (2013).

60. H. Cheng, R. L. Edwards, J. Hoff, C. D. Gallup, D. A. Richards, Y. Asmerom, The half-lives of uranium-234 and thorium-230. *Chemical Geology* **169**, 17–33 (2000).

61. J. C. Hellstrom, U–Th dating of speleothems with high initial 230Th using stratigraphical constraint. *Quaternary Geochronology* **1**, 289–295 (2006).

62. D. Scholz, D. L. Hoffmann, StalAge – An algorithm designed for construction of speleothem age models. *Quaternary Geochronology* **6**, 369–382 (2011).

63. S. F. M. Breitenbach, K. Rehfeld, B. Goswami, J. U. L. Baldini, H. E. Ridley, *et al.*, COnstructing Proxy Records from Age models (COPRA). *Clim. Past* **8**, 1765–1779 (2012).

64. E. J. Hendy, P. J. Tomiak, M. J. Collins, J. C. Hellstrom, A. W. Tudhope, *et al.*, Assessing amino acid racemization variability in coral intra-crystalline protein for geochronological applications. *Geochimica et Cosmochimica Acta* **86**, 338–353 (2012).

65. D. Scholz, D. L. Hoffmann, J. C. Hellstrom, C. B. Ramsey, A comparison of different methods for speleothem age modelling. *Quaternary Geochronology* **14**, 94–104 (2012).

66. R. N. Drysdale, G. Zanchetta, J. C. Hellstrom, A. E. Fallick, J. Zhao, Stalagmite evidence for the onset of the Last Interglacial in southern Europe at 129 ± 1 ka. *Geophys. Res. Lett.* **32**, 1–4 (2005).

67. K. Ludwig, *User's Manual for Isoplot 3.75 A Geochronological Toolkit for Microsoft Excel* (2012), pp. 1–75.

68. E. Roeckner, G. Bauml, L. Bonaventura, R. Brokopf, M. Esch, *et al.*, A. Tompkins, The atmospheric general circulation model ECHAM5 - Part I: Model description. *Max Planck Institute for Meteorology*, 1–140 (2003).

69. V. Brovkin, T. Raddatz, C. H. Reick, M. Claussen, V. Gayler, Global biogeophysical interactions between forest and climate. *Geophys. Res. Lett.* **36**, L07405 (2009).

70. S. J. Marsland, H. Haak, J. H. Jungclaus, M. Latif, F. Röske, The Max-Planck-Institute global ocean/sea ice model with orthogonal curvilinear coordinates. *Ocean Modelling* **5**, 91–127 (2003).

71. W. D. Hibler, A Dynamic Thermodynamic Sea Ice Model. *Journal of Physical Oceanography*, 815–846 (1979).

72. Z. Liu, B. L. Otto-Bliesner, F. He, E. C. Brady, R. Tomas, *et al*., J. Cheng, Transient Simulation of Last Deglaciation with a New Mechanism for Bolling-Allerod Warming. *Science* **325**, 310–314 (2009).

73. L. Menviel, A. Timmermann, O. E. Timm, A. Mouchet, Deconstructing the Last Glacial termination: the role of millennial and orbital-scale forcings. *Quaternary Science Reviews*, 1–18 (2011).

74. H. W. Arz, F. Lamy, A. Ganopolski, N. Nowaczyk, J. Pätzold, Dominant Northern Hemisphere climate control over millennial-scale glacial sea-level variability. *Quaternary Science Reviews* **26**, 312–321 (2007).

75. M. Siddall, E. J. Rohling, W. G. Thompson, C. Waelbroeck, Marine isotope stage 3 sea level fluctuations: Data synthesis and new outlook. *Rev. Geophys.* **46**, 109–29 (2008).

76. J. Ahn, E. J. Brook, Atmospheric CO2 and Climate on Millennial Time Scales During the Last Glacial Period. *Science* **322**, 83–85 (2008).

77. S. O. Rasmussen, K. K. Andersen, A. M. Svensson, J. P. Steffensen, B. M. Vinther, *et al*., M. E. Hansson, U. Ruth, A new Greenland ice core chronology for the last glacial termination. *Journal of Geophysical Research: Atmospheres* **111**, 527 (2006).

78. D. Liu, Y. Wang, H. Cheng, R. L. Edwards, X. Kong, *et al*., Sub-millennial variability of Asian monsoon intensity during the early MIS 3 and its analogue to the ice age terminations. *Quaternary Science Reviews* **29**, 1107–1115 (2010).

79. Wang, H. Cheng, R. L. Edwards, Z. An, J. Y. Wu, *et al.*, A High-Resolution Absolute-Dated Late Pleistocene Monsoon Record from Hulu Cave, China. *Science* **294**, 2345–2348 (2001).

80. X. Jiang, X. Wang, Y. He, H.-M. Hu, Z. Li, *et al.*, Precisely dated multidecadally resolved Asian summer monsoon dynamics 113.5-86.6 thousand years ago. *Quaternary Science Reviews* **143**, 1–12 (2016).

81. A. Berger, M. F. Loutre, Insolation values for the climate of the last 10 million years. *Quaternary Science Reviews* **10**, 297–317 (1991).

82. F. W. Cruz Jr., S. J. Burns, I. Karmann, W. D. Sharp, M. Vuille, Reconstruction of regional atmospheric circulation features during the late Pleistocene in subtropical Brazil from oxygen isotope composition of speleothems. *Earth and Planetary Science Letters* **248**, 495–507 (2006).

Acknowledgements: We thank all authors of the published speleothem records who made their data available online, shared their data or provided further information about their records. **Funding:** E.C.C. is supported by an Australian Government Research Training Program Scholarship. J.C.H. was supported by an Australian Research Council Future Fellowship (FT130100801). E.C. is funded by the European Union's Seventh Framework Program for research and innovation under the Marie Skłodowska-Curie grant agreement no. 600207. S.O.R. and E.C. acknowledge the support of the Carlsberg Foundation. X.Z. is supported by Helmholtz Postdoc Program (PD-301) and Qingdao National Laboratory for Marine Science and Technology (QNLM201703). D.F. was supported by the Swiss National Science Foundation (PP002-110554/1). E.W. is supported by a Royal Society professorship. **Author contributions:** R.N.D., D.F. and E.W. proposed the initial research idea. E.C.C. collated and standardised the data sets with assistance from J.C.H. and R.N.D. The analysis and interpretation of the results was performed by E.C.C., R.N.D. and J.C.H. with input from all authors. X.H. designed and performed the model simulations. E.C.C. led the write up of the manuscript with contributions from all authors. **Competing interests:** The authors declare no competing interests; and **Data and materials availability:** The data will be made available at the time of publication.

Supplementary Materials:

Materials and Methods

Figs. S1 to S8

Tables S1 to S4

Captions for Data S1 to S5

References *(59-80)*

Science
AAAS

Supplementary Materials for

Synchronous timing of abrupt climate changes during the last glacial period

Ellen C. Corrick[1,2*], Russell N. Drysdale[1,2], John C. Hellstrom[3], Emilie Capron[4,5], Sune Olander Rasmussen[5], Xu Zhang[6,7], Dominik Fleitmann[8], Isabelle Couchoud[2,1], Eric Wolff[9]
Correspondence to: e.corrick@student.unimelb.edu.au

This PDF file includes:

Other Supplementary Materials for this manuscript include the following:

Materials and Methods

1. Selection of speleothem records

Speleothem stable isotope records falling within the interval 119 to 12.5 kyr BP were identified from peer-reviewed literature. For each record, the stable-isotope depth series and the uranium-thorium (U-Th) age data were sourced from either the publication, the NOAA palaeoclimate database (https://www.ncdc.noaa.gov/data-access/paleoclimatology-data/datasets/speleothem) or by personal communication with authors. Records were excluded from the comparison in cases where all data could not be obtained.

The records were screened in two steps: first, to identify suitable records for reprocessing (see below) and, second, to evaluate the ability to identify individual events in each speleothem once the data have been reprocessed. The following criteria were used to select records for reprocessing: i) continuous temporal coverage over the entirety of one or more formally designated *(3)* stadial-to-interstadial transitions; ii) temporal resolution consistently better than at least three proxy data points per thousand years (it is important to note that temporal resolution may be highly variable within a speleothem due to changes in growth rate – this constraint was used initially to exclude very low-resolution records but does not guarantee that an event can be detected in the record); and iii) a chronology established by direct U-Th dating and having at least three age determinations over a continuous growth section (this being necessary to obtain an accurate representation of the depth-age relationship). A total of 71 records met the above criteria as of mid 2017. It is important to note that these criteria comprise the first-stage of screening, and whilst serving a useful purpose in identifying records for inclusion in the comparison, we are not implying that these criteria are sufficient to detect an interstadial in all cases. Instead, these are the base conditions a record must meet for further consideration.

Following reprocessing, the exclusion or inclusion of a record was judged on an event-by-event basis according to the event characteristics discussed in section 3. Events were only identified in sections of each record that exhibited a temporal resolution of at least three data points per thousand years and a chronological precision better than 3.5% over the transition. This additional criteria of a having a precision of better than 3.5% was determined as the lowest level of precision that would provide suitable constraint to the intra- and inter-regional age calculations. Each reprocessed record is represented in Fig. S3 (temporal span only) and Data S3 (full oxygen isotope profile) showing in colour the sections that fulfil these criteria (grey sections do not fulfil these criteria). We stress that meeting these criteria does not guarantee an event identification is possible.

The vast majority of qualifying records are from the Asian Summer Monsoon (ASM), South American Monsoon (SAM) and European-Mediterranean (EM) regions. Given the focus of our work on the investigation of regionally coherent speleothem records and the importance of making robust comparisons between regions, we restricted our study to records from these three regions. Based on the number of available speleothem records, it is not possible to subdivide these regions into smaller areas for more in-depth intra-regional comparisons. The full list of records is provided in Table S1.

2. Standardisation of speleothem records

All records were standardised and a revised chronology for each proxy time series was constructed to overcome potential biases originating from methodological inconsistencies in the calculation of U-Th ages and in the modelling of depth-age relationships in order to permit robust comparisons to be made. To standardise the data, the activity ratios and 2σ uncertainties of (^{230}Th/^{238}U), (^{234}U/^{238}U) and (^{232}Th/^{238}U), or other appropriate isotope concentrations or ratios to reconstruct these values, were required.

2a. Recalculation of uranium-thorium ages. All ages were recalculated using the most recent estimates of the decay constants of ^{234}U (λ_{234} = 2.82206 x 10^{-6}) and ^{230}Th (λ_{230} = 9.1705 x 10^{-6}) *(59)*. This led to a shift to slightly younger ages (generally between 0.1 – 0.2%) for records published prior to 2013 or that otherwise used previous estimates of the decay constants *(60)*.

Detrital thorium correction is essential to U-Th dating and can be performed by estimation of the initial ^{232}Th/^{230}Th activity ratio using one of several potential methods *(61)*. The ^{232}Th/^{230}Th activity ratio used in the original publication was preserved when based on isochron techniques or stratigraphic constraints specific to that setting. By far the most common approach assumes a bulk Earth ^{232}Th/^{230}Th activity ratio of 0.82 ± 0.41 (equivalent to an atomic ratio of 4.4 ± 2.2 x 10^{-6}), derived from the bulk Earth ^{232}Th/^{238}U atomic ratio of 3.8 x 10^{-6}, but this does not encompass the full range of ^{230}Th/^{232}Th variability observed in speleothems *(61)*. Where the bulk Earth value had been assumed, it was replaced by a ^{232}Th/^{230}Th activity ratio of 1.5 ± 1.5 which has been shown to be a more appropriate estimate where no prior information is available, given the range of values seen in speleothems *(61)*. Where necessary, stratigraphic constraints *(61)* were used to refine this to a speleothem-specific estimate. In all other cases, where it was otherwise unclear what (or if any) correction had been performed, a ^{232}Th/^{230}Th activity ratio of 1.5 ± 1.5 (2σ) was applied. Shifting to this correction value resulted in a slightly larger correction leading to slightly younger corrected ages for samples with a significant detrital component. The uncertainty associated with correction for detrital thorium was fully propagated to the final age.

All recalculated ages are expressed as 'thousands of years before present' where 'present' is the year AD1950. U-Th ages are calculated in years before the day on which the U-Th measurements were made. In cases where the year of measurement was not given in the literature, it was assumed to be two years prior to the date of publication of the record. This was performed for consistency and makes an infinitesimal difference to the final calculated ages or any comparisons.

2b. Remodelling of depth-age relationships. Methods used in speleothem science for modelling depth-age relationships include simple linear interpolation or regression to more sophisticated speleothem-specific algorithms based on Monte-Carlo simulations, such as StalAge *(62)*, COPRA *(63)* or the finite-positive-growth-rate model *(64, 65)*. Different methods may return slightly different depth-age relationships and thus chronologies, although such differences are generally small in the more densely dated speleothems *(65)*. Linear interpolation or regression was the most commonly reported technique used for the records considered herein, despite their inability to model realistic growth-rate changes or account for interpolation uncertainty between age determinations. To overcome modelling inconsistencies, all depth-age relationships were reprocessed using the finite-positive-growth-rate model (described in the first version *(66)* and current version *(64)* developed within *Wavemetrics Igor Pro.* This model is specifically developed to model speleothem growth, accounts for sampling depth uncertainty and enables the extraction of the probability distribution of the modelled age for any depth. At the time of publication of this

manuscript, no other available model possessed all such capabilities. Briefly, a least-squares best-fit age sequence is fitted through the U-Th age determinations of a speleothem, subject to the constraint that average growth rate between them must be finite, positive and relatively invariant. A user-adjustable parameter, *growth rate tolerance*, adjusts the weighting with which the model attempts to minimise growth-rate variability, such that values less than one favour reduced growth-rate variability and values greater than one force the model close to the central values of each age determination. Growth rate tolerance was adjusted (within a defined uncertainty range) in each case to best reduce "steps" in which growth rate would otherwise spike between adjacent inverted age determinations, and has little effect elsewhere.

The finite-positive-growth-rate model also accounts for sampling uncertainty in the depth dimension and for interpolation uncertainty between two age determinations (such that, by default, growth rate is allowed to vary over an order of magnitude at all time scales). Where a measure of sampling-depth uncertainty was not directly provided in the publication, an estimate was made based on the description of the sampling technique, sample mass used or from images of the speleothem showing sample locations. Unless it was otherwise stated or clearly obvious in images, a single depth uncertainty estimate was applied to all age determinations for a single speleothem. Sampling depth was taken as the distance from the top of the stalagmite in millimetres. Any hiatuses, either described in the original publication or inferred from depth-age models, were observed in the construction of the chronology by, in most cases, treating each continuous growth interval independently. Each model is normally run as a 10,000-iteration Monte-Carlo simulation in which for each iteration each age determination is randomised within its uncertainty, along with growth-rate tolerance, which also has a user-assigned uncertainty. The resulting population of depth-age models gives a median age at any depth in the speleothem and allows extraction of probability distributions with 95% confidence intervals.

Outlier detection and exclusion was performed independently of decisions made in the original publication and based on visual determination of disagreement of an age and its uncertainty with the depth-age model evolved from surrounding age determinations. Where multiple ages were provided for a single depth increment, the most precisely constrained age was used, if it did not appear to be inaccurate for any other reason. The depth-age models produced for each data set are illustrated in the Supplementary Materials Data S2. In several cases, it was determined that a reliable depth-age model could not be produced from the available data due to multiple ages falling out of stratigraphic order, suggesting open-system behaviour or diagenesis in the speleothem (as per *(49)*). In such cases, the record was excluded from the comparison.

There is discussion in the literature as to the extent to which depth-age modelling can be automated, and to which skilled human adjustment of parameters, such as growth rate weighting and outlier rejection, is required *(65)*. The human decision-making approach used here requires that we develop depth-age models independently of their associated proxy records to avoid the possibility of bias, so the models were finalised prior to moving to the next step.

Following finalisation of each depth-age model and uncertainty envelope, an age and uncertainty interval was extracted at the depth of each oxygen isotope measurement. Models are not extrapolated to proxy isotope data falling outside the range of the depth interval covered by the first and last age determination. The standardisation of all data sets per this methodology led to some differences between revised and published chronologies. Differences were most often observed where a linearly interpolated model created very abrupt growth-rate changes, while the finite-positive-growth-rate model allowed for a smoother growth-rate change; or where the

application of a revised detrital-thorium correction to samples with a significant detrital component led to larger corrections, although in such cases the uncertainty associated with the correction was also considerably larger. Any differences were usually small and within the age uncertainty envelope of the final model (see examples in Fig. S5).

3. Identification of interstadials

Attempt at event identifications were made in sections of the reprocessed records that fulfilled the criteria of having at least three data points per thousand years and a chronological precision better than 3.5% (represented as coloured sections in Data S3 and Fig. S3). Interstadial onsets were identified where a clear transition could be seen in the speleothem $\delta^{18}O$ record that was structurally similar to that seen in Greenland ice (i.e. the record showed clear evidence of relatively stable stadial conditions, followed by a period of transition to interstadial conditions). This took account of the behaviour of the speleothem $\delta^{18}O$ over both short (decadal/sub-decadal) and longer time scales in order to differentiate, for example, between longer-term changes driven by insolation *(39)* and from abrupt transitions. In most cases, identification of individual DO events was inferred by authors of the original publications. Here we sought to define the timing of interstadial onsets in each record. We adopted the method utilised in developing the event stratigraphy in the Greenland ice cores *(3)* in order to enable direct comparison to the event ages produced therein. Each interstadial onset is taken to be the '*the first data point of the steep part that clearly deviates from the base-line level preceding the transition' (3)*. In the application of this method, the baseline conditions are considered to be the proxy values throughout the stadial (or sub-stadial) period preceding the interstadial (Fig. S2**)**. The timing of the interstadial onset is defined as the age assigned to the first data point of the interstadial transition that 'exceeds' (this may be more or less negative depending on the direction of the $\delta^{18}O$ response) the 'maximum' value recorded during the stadial period. In this sense, the timing of the interstadial onset is defined as the point at which the proxy response exceeds the level of variability observed during the previous stadial period. See Fig. S2 for a depiction of this method. However, in applying this rule strictly we found that the position of the point within the interstadial transition (i.e. peak, mid-point, first rise) often varied between different speleothem records due to differences in their resolution and noise. To ensure that the comparison of the timing of a given event was based on a consistent positioning between speleothem records, it was occasionally necessary to shift the point to a position structurally similar to that of the event's assigned position in NGRIP (*3*). All such changes fell well within the uncertainty of the age estimates. All event identifications are shown in Data S3.

In assigning interstadial numbers to the transitions, we studied the record across its length to identify the sequence of events, based on characteristic features such as shape, duration and magnitude. We have only included interstadial onsets where both the assignment of interstadial numbers, and identification of the interstadial onset itself could be accomplished with confidence. Statistical methods to identify the onset of interstadial transitions were found to be difficult to implement consistently to all speleothem records due to the variability in resolution of the speleothem data and the short duration of many interstadials. To the best of our knowledge, no automated technique has been successfully developed to identify individual events within a sequence (i.e. automatically assign event numbers).

Of the 53 events described by ref. (*3*), we excluded seven (GI-1a, 1c1, 1c3, 2.1, 2.2, 8a and 20a) from the comparison, deeming them too subtle to be detected adequately in the speleothem records.

In all cases, $\delta^{18}O$ was chosen as the palaeoclimate proxy in the speleothem record because of its ability to act as a rapid atmospheric tracer (as opposed to carbon isotopes, which can respond to vegetation/soil CO_2 changes that may occur over longer time periods). For each event, identification of its age and $\pm 2\sigma$ uncertainty was obtained from the depth-age model. In total, 63 individual speleothem records were included in the final compilation (see Table S1 for full list).

The recording of a palaeoclimate signal in a speleothem is very different compared to the surface of an ice sheet (and ultimately in an ice core), even for profound climate perturbations such as DO events. Many factors combined to influence the oxygen isotope signal in speleothems, including climate and environmental effects in the epikarst above the cave, and the physical conditions within the cave (e.g. PCO_2, humidity) during speleothem formation. These processes are site, and often speleothem, specific and may vary through time at a single site. Therefore, a speleothem may clearly record one interstadial but not another. Speleothem growth rate is also highly variable, meaning sections of a record may have sufficient resolution to clearly resolve one interstadial onset whereas others may go undetected. For example, for many of the records that met the criteria to attempt event identification, event identification was not possible due to: lack of sufficient resolution to record an event (e.g. many short lived events require decadal or sub-decadal resolution to be resolved); complacency in the speleothem signal due to competing processes that dampen the local isotope response; insufficient confidence to differentiate between neighbouring events (e.g. if a difference between 14e and 14c cannot be clearly discerned); structural differences with NGRIP that add uncertainty to the event ID or otherwise a lack of confidence in the event ID. This explains why many speleothem records represented in Fig. S3 cover certain interstadials yet positive event identification could not be made. Such variability in the preservation of the signal in speleothems is not unexpected; this is the nature of speleothems as palaeoclimate archives, and it clearly highlights the importance of drawing on numerous records. The reader is directed to Data S3 for the full isotope record of each speleothem included in the comparison.

4. Testing of the synchrony of interstadial onsets

For each region (and finally between regions), we take the error-weighted mean (EWM) age as

Eq. 1

$$t_{ewm} = \frac{\sum w_i t_i}{\sum w_i}$$

Where the weights are given by

Eq. 2

$$w_i = \frac{1}{\sigma_i^2}$$

Uncertainty in t_{ewm} is then calculated as

Eq. 3

$$\sigma_{t_{ewm}} = \frac{1}{\sqrt{\sum w_i}}$$

For each individual speleothem age estimate, age uncertainty (σ_i) was taken as the average of the plus and minus errors obtained from the depth-age model.

The Mean Square Weighted Deviation (MSWD) statistic *(47, 48)* was used to test the synchrony in the timing of interstadial onset between different records. This statistic is more broadly known as the reduced chi-square statistic (χ^2_{red}), but is commonly used in geochronology to test the reproducibility of multiple ages taken from a single crystal or rock layer. The MSWD compares the measured differences between the individual ages (t_i) and the error weighted mean (t_{ewm} see Eq. 1) to the expected difference that is indicated by the variance (σ^2), and is calculated here as

Eq. 4

$$\chi^2_{red} = \text{MSWD} = \frac{1}{n-1}\sum_{i=1}^{n}\frac{(t_i - t_{ewm})^2}{\sigma^2_{t_i}}$$

Where t_i may represent either (1) individual speleothem age estimates (when testing intra-regional synchrony), or (2) regional EWM ages (when testing inter-regional synchrony and there are multiple records from a region).

A scatter of ages that agrees with that expected from the estimated uncertainties yields a MSWD approximately equal to 1, with the MSWD tending closer towards 1 with increasing *n*. The acceptable range of the MSWD for the given degrees of freedom ($n - 1$) at the 95% confidence interval is given in ref. *(48)* (for example, the range is 0.00 – 2.61 at $n = 4$ and 0.14 – 2.05 at $n = 8$). Here we applied the MSWD to test if the spread in the timing of the onset of an interstadial between different speleothem records can be explained by analytical uncertainty alone (MSWD within the accepted range and interpreted as the synchronous timing of the onset within the bounds of uncertainty) or if there are differences in the timing of the interstadial onset that exceed that which can be attributed to analytical uncertainty alone (MSWD > accepted range).

In the comparison, we used only interstadial onset timings with a precision better than 3.5%. We first tested the synchrony of the onset of an interstadial within each of the three regions, and then between regions. We assumed that within a region an abrupt change should be recorded synchronously given that the records should all be responding to the same climate forcing. This assumption enables us to test the quality of the different records. In the majority of cases, there is good agreement between records within a region to indicate the synchronous timing of the interstadial onset. Where the within-region MSWD exceeds the expected range, the region was marked as unresolved, unless the identification and exclusion of an outlying record could be justified. In several cases we found some individual records to be anomalous compared to multiple records from the same region. This highlights the importance of not relying on single individual speleothem records, no matter their precision, due to a variety of issues that may afflict the chronology.

To test the synchrony between regions, we calculated the MSWD based on the EWM and uncertainty for each region. We then obtain a combined speleothem EWM and uncertainty for the event. The calculation of both the MSWD and EWM was performed within *Isoplot*, a Visual Basic add-in for Microsoft Excel *(67)*.

5. Regression

The non-parametric robust regression test, implemented in *Isoplot*, was used to determine the slope and *y*-intercept of the bivariate plot of speleothem ages (±2σ) versus GICC05 ages (±MCE) (*x* and *y* respectively). Due to the tendency for age errors to increase with age (monotonically in the case of GICC05), the residuals are not normally distributed and therefore a parametric test (least-squares) is inappropriate.

6. Model information

6a. Fully coupled atmosphere-ocean circulation model

We employ a comprehensive fully coupled atmosphere-ocean general circulation model (AO-GCM), COSMOS (ECHAM5-JSBACH-MPIOM) to study the spatial synchrony of climate changes during DO events (Table S4; Fig. S7). The atmospheric model ECHAM5 *(68)*, complemented by a land surface component JSBACH *(69)*, is used at T31 resolution (~ 3.75°), with 19 vertical layers. The ocean model MPIOM *(70)* including sea-ice dynamics that is formulated using viscous-plastic rheology *(71)*, has a nominal resolution of 3° × 1.8° in the horizontal, with 40 uneven vertical layers. This model has successfully simulated DO-type climate changes under glacial climate background conditions. Distinguishing it from other AOGCMs that mainly employed freshwater perturbations to mimic DO events *(52, 72, 73)*, this model can further simulate abrupt changes in glacial AMOC modes by gradual changes in ice sheet and/or atmospheric CO_2 (*19*, *20*), of which results are in good agreement with paleoclimate reconstructions. This indicates that this model captures the large-scale dynamics of DO events (and the AMOC changes in which they are expressed), and so is a reliable platform to study the associated spatial phasing of the climate changes.

6b. Composite of simulated stadial–interstadial climate anomalies

Inter-comparison of climate responses to the AMOC changes under similar/identical forcing scenarios is often made to assess common features and dynamics among models *(53)*. Instead, here we compare the climate responses to different forcing scenarios in one climate model. Given the identical physical scheme in the model, this enables us to identify the robust common features in response to a broad range of forcing scenarios that represent most of triggering dynamics of DO events (Fig. S7). In addition, this will help us to evaluate whether the regions represented by speleothem records compiled in this study are representative of climate changes during these events.

In this comparison, we collect equilibrium climate states from two hosing experiments *(52)*, two sets of CO_2-single forcing experiments *(20)*, and three sets of ice sheet single forcing experiments *(19)* (Table S4). Given that responses of the AMOC to various forcing scenarios could be different, we define a simple algorithm to account for the weight of the AMOC changes in the climate anomalies:

$$V_w = \frac{\delta v}{\delta \varphi}$$

$\delta\varphi$ and δv are the anomalies of AMOC strength and climate variables between different AMOC modes, and so V_w represents the $\delta\varphi$-weighted climate anomalies. We assume that climate responses to AMOC changes under different forcing scenarios are linear over a long-term

equilibrium time scale (~1000 years). Therefore, the overall composite field C_v can be obtained by:

$$C_v = \frac{1}{n}\sum_{i=1}^{n}\frac{\delta v_i}{\delta \varphi_i}$$

In which n (=7) is the number of climate anomalous fields.

As shown in Fig. S7, responses of annual mean air temperature and precipitation are coherent across different scenarios and consistent with paleoclimate reconstructions (*19*, *20*), although the background conditions are also different. This highlights the critical role of AMOC changes, irrespective of forcing factors and climate backgrounds, in shaping global climate changes during DO events. This further highlights that the global synchrony in this study is difficult to explain in terms of the underlying mechanisms of these events. Since key processes that trigger AMOC changes happened at different regions under different forcing scenarios *(18-20, 55)*, well-dated, high-resolution records from these key regions will be very instructive and crucial to identify the underlying dynamics of DO events.

6.c Phasing analysis in hosing experiment

To study global climate synchrony during DO events, we conducted long-term North Atlantic hosing experiments *(52)*, in which a ~0.2Sv freshwater flux was imposed to the Ruddiman Belt for 1000 years to mimic a cold 'stadial' climate state. As the freshwater flux is removed at the 1001st model year, the AMOC starts increasing instantly and reaches its 'interstadial' state within a century. Since we focus on the abrupt AMOC recovery phase, we treat the 1001st model year as the 1st year in Fig. 4, and only show the 500 years before and after it. Whilst other forcing factors (e.g. ice-sheet height and atmospheric CO_2) are also able to mimic DO-type abrupt AMOC changes (*19*, *20*), these will introduce additional uncertainties to assess the role of AMOC changes alone on the spatial synchrony, due to: 1) the uncertainty of ice volume changes during abrupt DO transitions *(74, 75)*; and 2) the apparent lack of coherence between DO transitions accompanied by evident CO_2 changes *(76)* (Fig. S6). Since our compilation represents the general characteristics of DO events in the last glacial period, we use the hosing experiment as a surrogate to quantify the spatial phasing of climate changes during abrupt AMOC recovery. A change-point algorithm implemented in *Matlab (58)* was used to determine the timing of the onset of changes through the simulated interstadial onset (Fig. 4B-K). This method uses a Bayesian least-squares approach to estimate the year (and the 95% uncertainties) when a parameter changes from one state to another. The 95% uncertainties are 15 years or less in all cases.

7. Use of Greenland ice-core data

We refer to the last glacial section of the Greenland NGRIP ice-core record (*2*) on the GICC05 and GICC05modelext chronologies *(32, 50, 77)* with all ages reported as thousands of years before 1950 (kyr BP). We take the Maximum Counting Error (MCE) as a 2σ (95%) age uncertainty. We use the latest *(3)* nomenclature and timing of interstadials and stadials, with age expressed in kyr BP.

Fig. S1. Determining the time interval and its uncertainty between consecutive interstadials in the annual-layer-counted section of the GICC05 chronology for NGRIP $\delta^{18}O$. The example of the time interval between GI 6 and GI 5.2 is shown. The uncertainty in the duration between events is the difference in the maximum counting error (MCE) at each transition. Thus, the interval and its uncertainty is 1,240 ± 80 years.

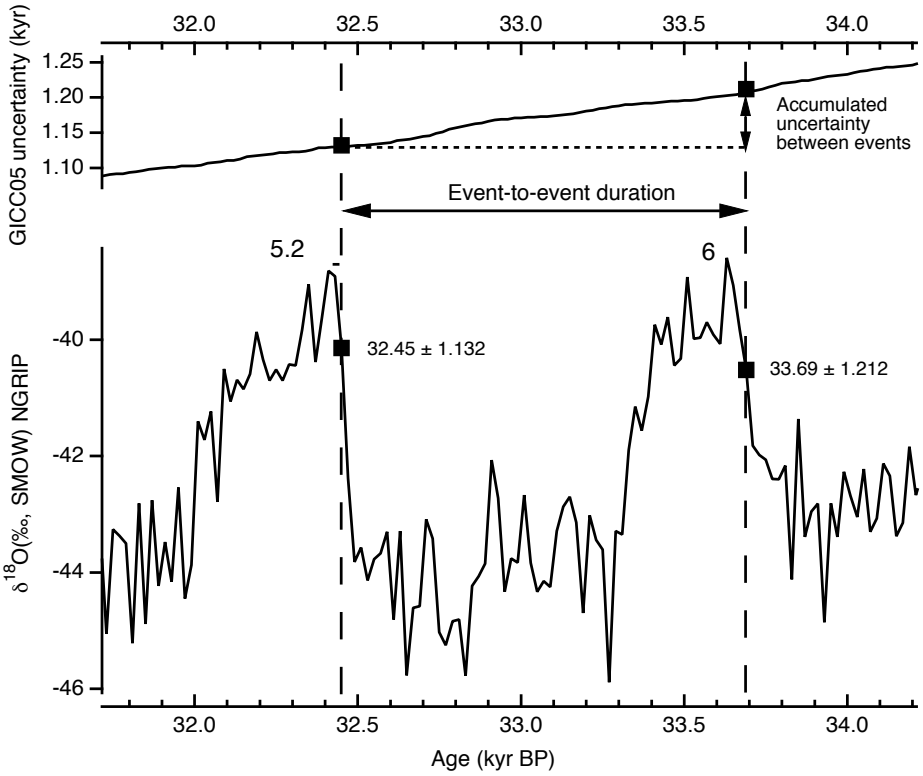

Fig. S2 An example of the interstadial onset identification method. The example is provided for several interstadials in the Pacupahuain Cave (PH2) record *(16)* and NGRIP *(2)*. Blue dashed lines indicate the baseline conditions preceding the abrupt transition. The timing of the event (black squares in PH2, red squares in NGRIP) is taken as the first data point that exceeds the baseline conditions, according to the method of ref *(3)*. In cases where the position of the event within a transition does not mirror that of NGRIP (grey dots), the event identification point was translated to a structurally similar position, as shown in the identification of interstadial 7c in PH2.

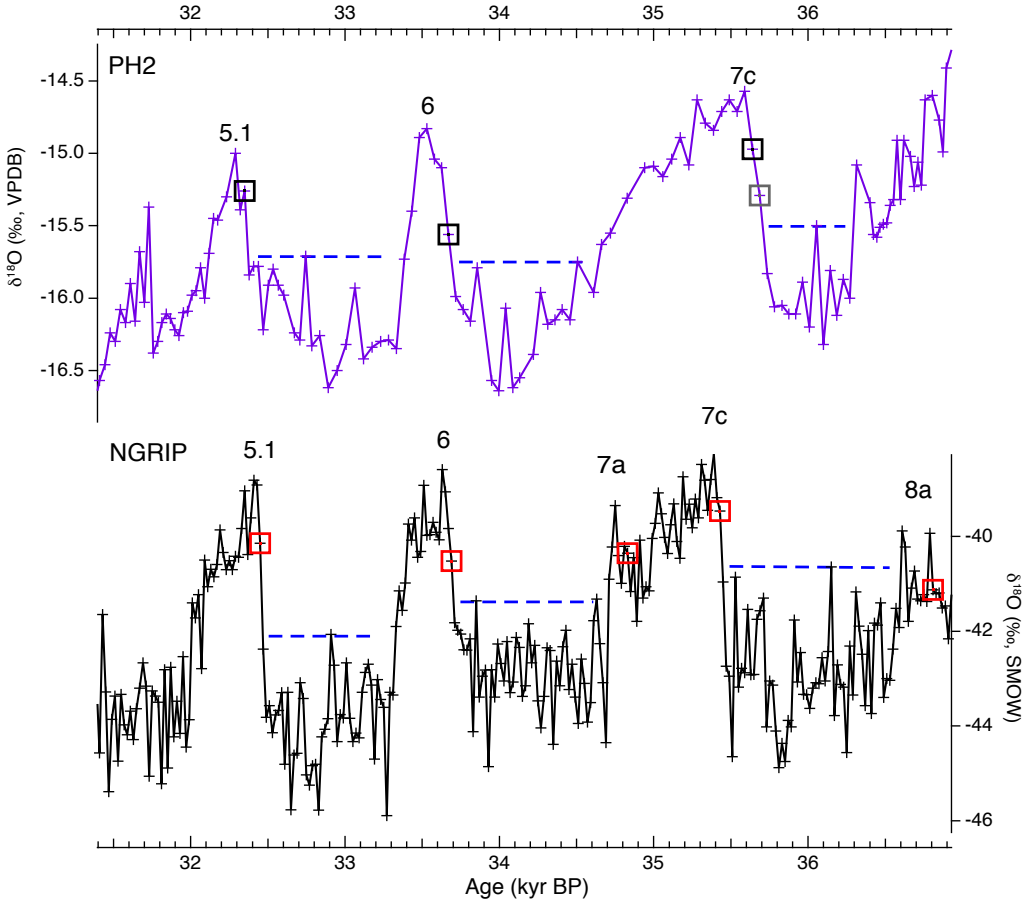

Fig. S3. The temporal span of the 63 speleothem records included in the compilation. Shown are sections of each record that meet the criteria as being suitable for event identification (at least three data points per thousand years and age precision better than 3.5%) *(34)*, colour coded by regional of origin (orange = EM, blue = ASM, purple = SAM). Sections of the records that do not meet these criteria are shown in dark grey. Although sections represented in colour do meet the above mentioned criteria this does not guarantee the record has sufficient resolution to detect certain interstadials, particularly the shorter-lived events, nor does it imply that the individual speleothem record may be sensitive to all interstadial changes. Therefore, a confident event identification is not possible at the intersection of every vertical light grey and horizontal coloured line. Light grey vertical lines represent the timing of interstadials as recorded in GICC05/GICC05modelext *(3)* for interstadial onsets included in the comparison. Sample codes are shown for each speleothem. See Table S1 for the full list of records and associated references and Data S3 full oxygen isotope record for each speleothem utilised in the compilation.

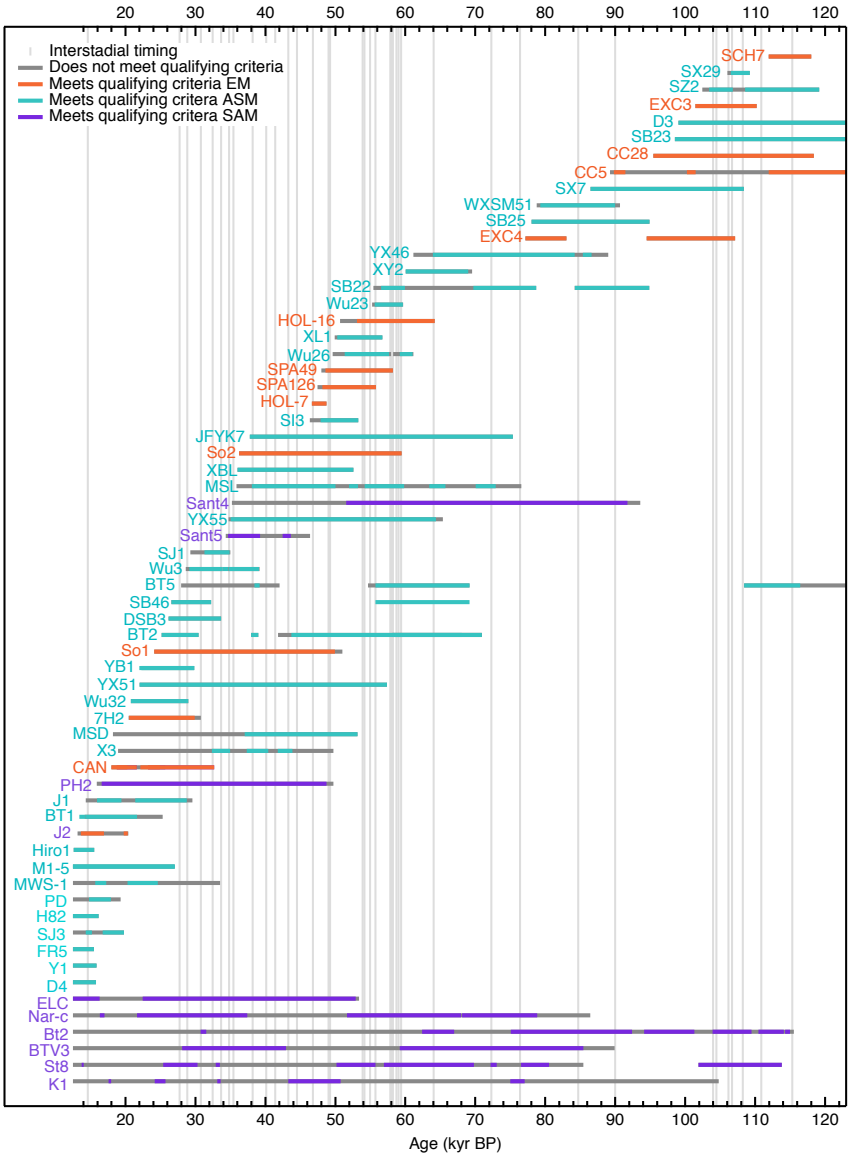

Fig. S4 Isotope plots showing the identification of specific interstadials in detail. Selected events at first appear equivocal in Fig. 2 and are shown here in more detail. A – interstadial 5.1 and 5.2; B - interstadial 7a and 7c; C - interstadial 14c and 14e; E-F interstadials 16 to 17 in stalagmite BT2 *(37)*, Wu23 *(78)* and MSL *(79)*; and G- interstadial 24.1a, .1c and .2 in SX29 *(80)*. Each record is shown on its own re-calculated age model *(34)* and is colour coded according to region (orange = Europe and Mediterranean; blue = Asian Summer Monsoon; purple = South American Monsoon). The age of each interstadial onset is indicated by a solid red square on the NGRIP $\delta^{18}O$ series (black curves; plotted on the GICC05 or GICC05modelext chronology) according to its position assigned by ref. *(3)*. The corresponding position of the events in each speleothem record is indicated by a solid black circle. Only records used in the final age calculation are shown. Error bars represent 2σ uncertainties. Lettering provides the sample code for each speleothem record. Refer to Table S1 for the full details and reference of each record.

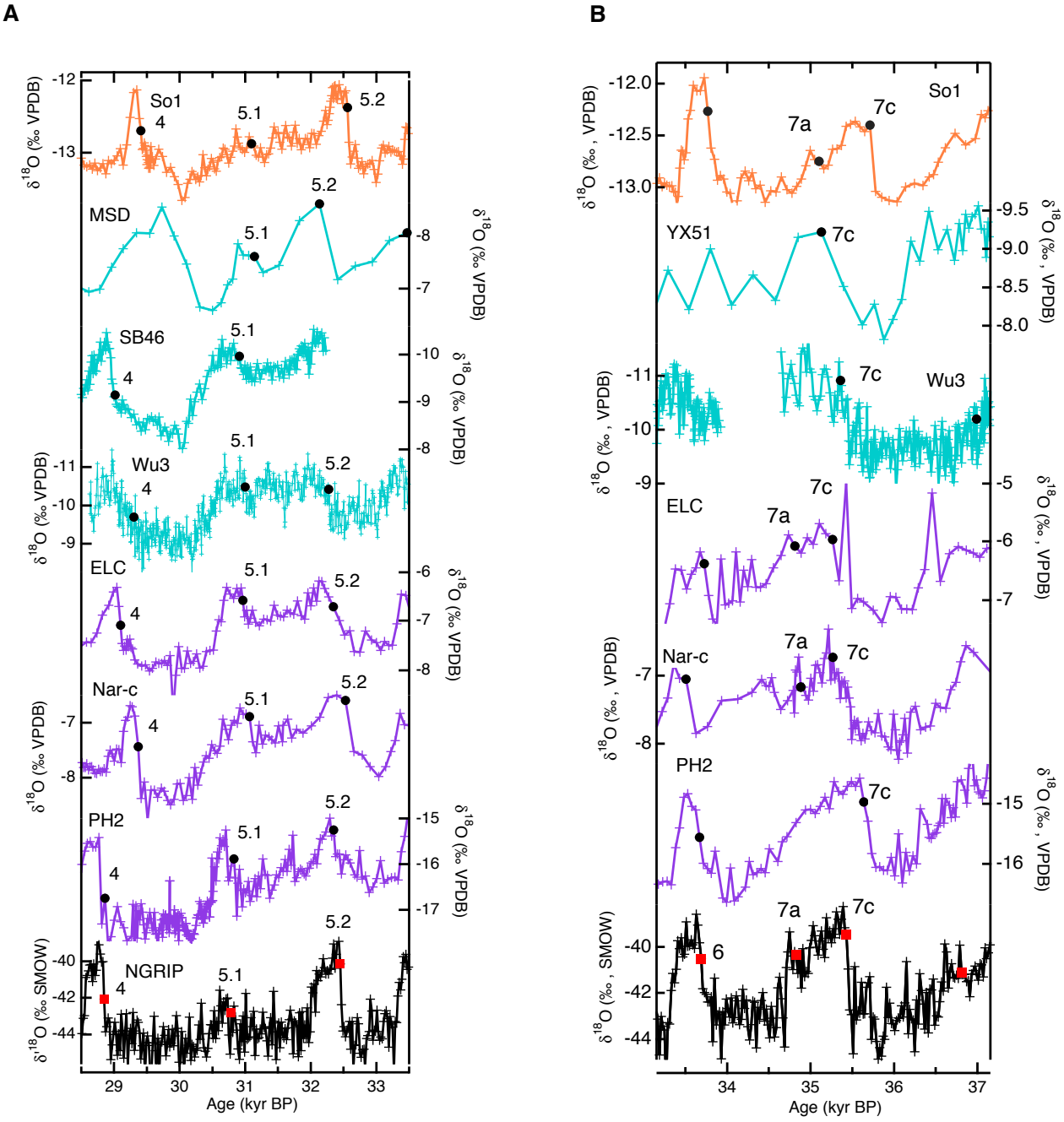
A
B
So1
MSD
SB46
Wu3
ELC
Nar-c
PH2
NGRIP
YX51
4
5.1
5.2
6
7a
7c
δ18O (‰ VPDB)
δ18O (‰ SMOW)
Age (kyr BP)

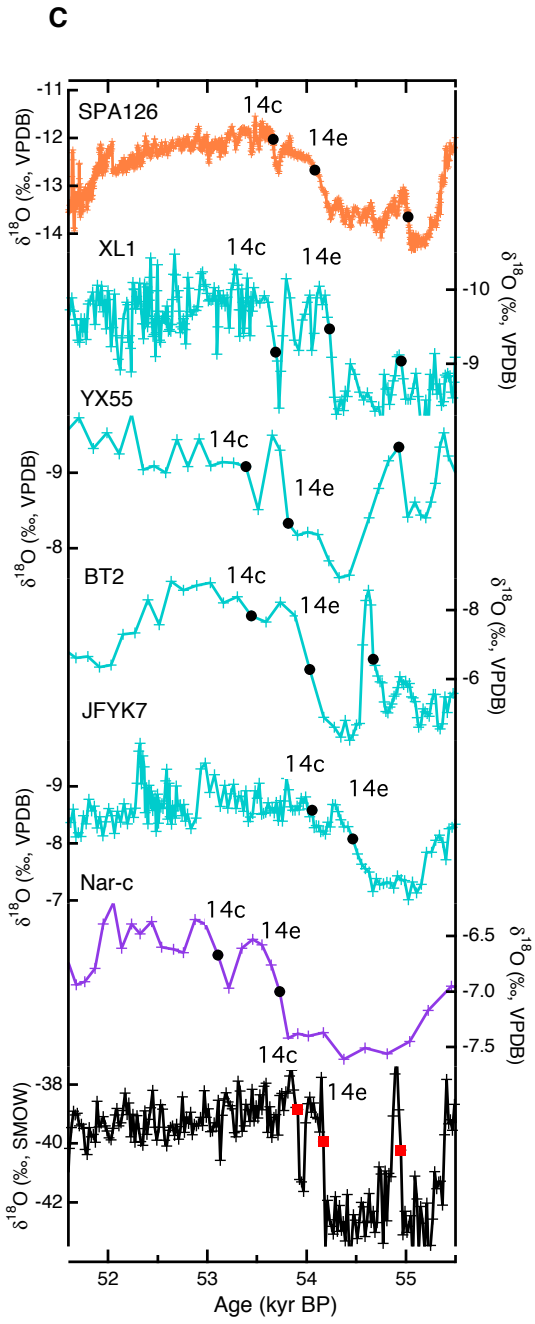
C
SPA126
14c
14e
XL1
YX55
BT2
JFYK7
Nar-c
δ18O (‰, VPDB)
δ18O (‰, SMOW)
Age (kyr BP)
52
53
54
55

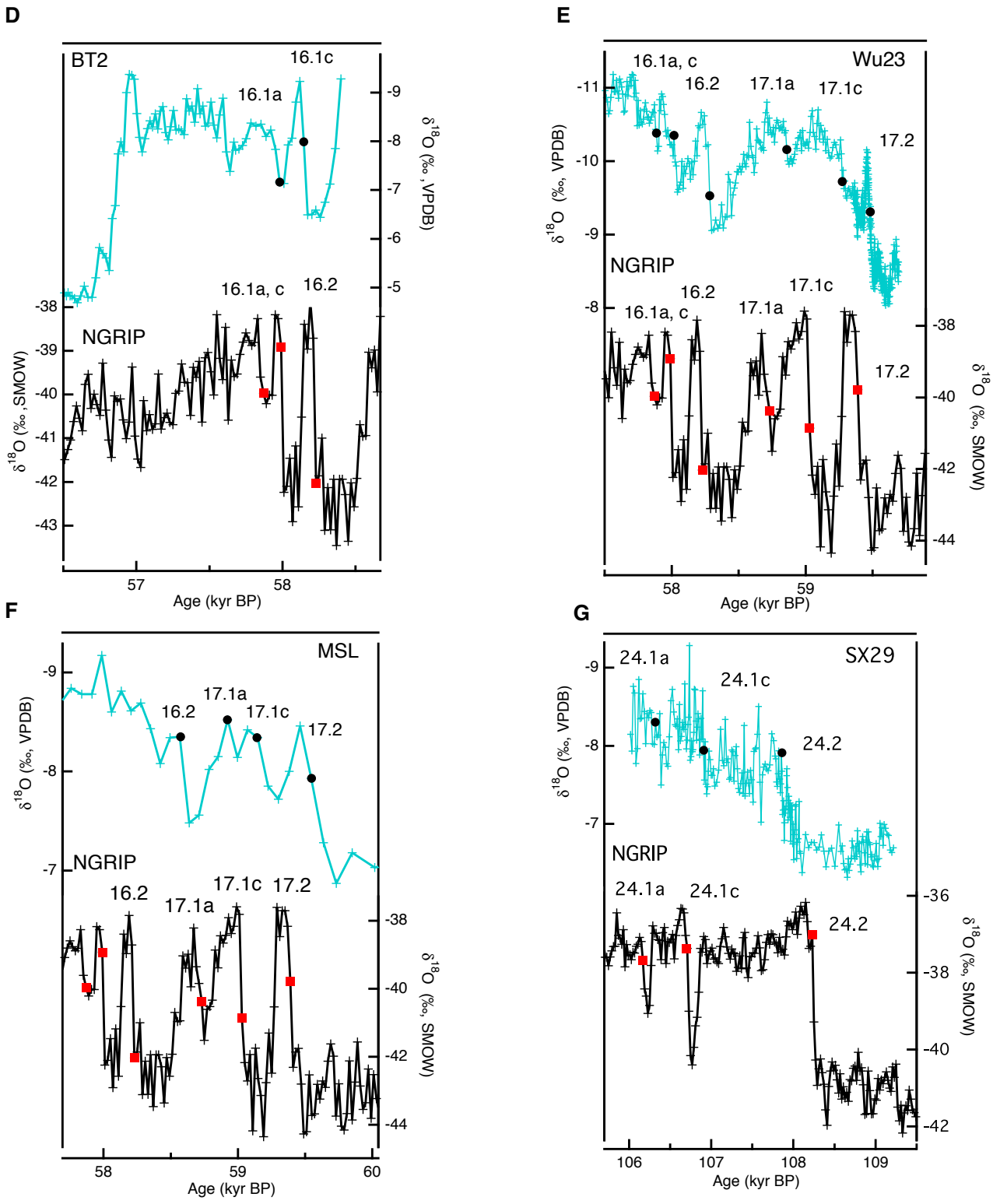
D
BT2
16.1c
16.1a
16.1a, c
16.2
NGRIP
δ18O (‰, SMOW)
δ18O (‰, VPDB)
Age (kyr BP)
E
Wu23
16.1a, c
16.2
17.1a
17.1c
17.2
NGRIP
δ18O (‰, VPDB)
δ18O (‰, SMOW)
Age (kyr BP)
F
MSL
16.2
17.1a
17.1c
17.2
NGRIP
δ18O (‰, VPDB)
δ18O (‰, SMOW)
Age (kyr BP)
G
SX29
24.1a
24.1c
24.2
NGRIP
δ18O (‰, VPDB)
δ18O (‰, SMOW)
Age (kyr BP)

Fig. S5. Probability density functions (pdfs) from individual speleothem records for interstadials shown to be synchronous between two or more records. The pdfs were obtained from the histogram of the distribution of potential ages at the speleothem depth attributed to the onset of the interstadial and derived from the corresponding depth-age model. Pdfs were produced using a 5-year bin width and by applying a 40- point moving average. The combined error-weighted-mean (EWM) age and 2σ uncertainty is shown as a black horizontal error bar. In cases where there are at least two records from a region, coloured error bars give the regional EWM ages and uncertainties. Text refers to the name of each speleothem. Refer to Table S1 for details of each record.

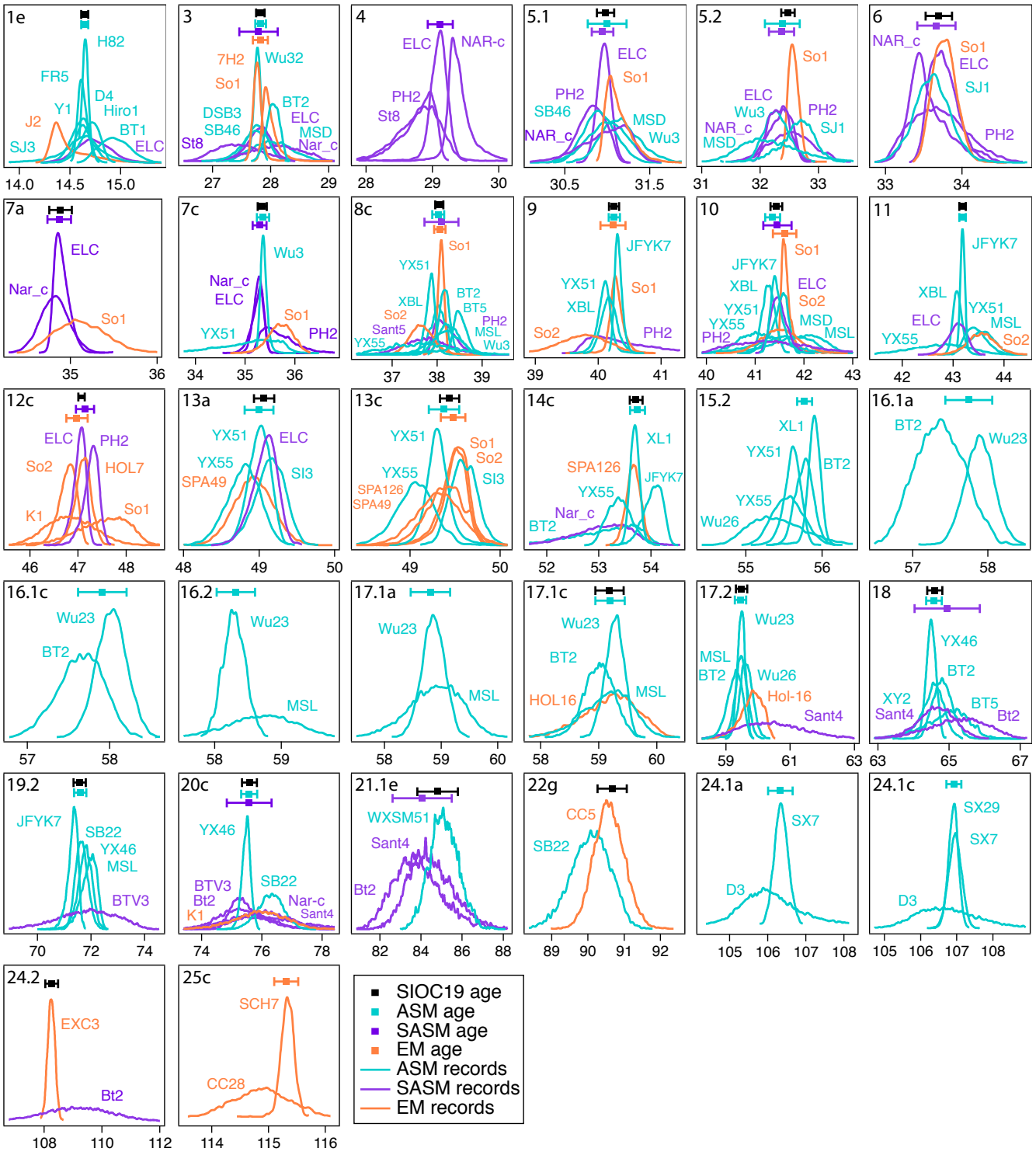
1e
H82
FR5
D4
Y1
Hiro1
J2
BT1
SJ3
ELC
14.0
14.5
15.0
3
7H2
Wu32
So1
BT2
DSB3
ELC
SB46
MSD
St8
Nar_c
27
28
29
4
ELC
NAR-c
PH2
St8
28
29
30
5.1
ELC
So1
PH2
SB46
MSD
NAR_c
Wu3
30.5
31.5
5.2
So1
ELC
Wu3
PH2
NAR_c
SJ1
MSD
31
32
33
6
NAR_c
So1
ELC
SJ1
PH2
33
34
7a
ELC
Nar_c
So1
35
36
7c
Wu3
Nar_c
ELC
So1
YX51
PH2
34
35
36
8c
So1
YX51
XBL
BT2
BT5
So2
PH2
Sant5
MSL
YX55
Wu3
37
38
39
9
JFYK7
YX51
So1
XBL
So2
PH2
39
40
41
10
So1
JFYK7
XBL
ELC
YX51
So2
YX55
MSD
PH2
MSL
40
41
42
43
11
JFYK7
XBL
YX51
ELC
MSL
YX55
So2
42
43
44
12c
ELC
PH2
So2
HOL7
K1
So1
46
47
48
13a
YX51
ELC
YX55
SI3
SPA49
48
49
50
13c
YX51
So1
So2
YX55
SI3
SPA126
SPA49
49
50
14c
XL1
SPA126
JFYK7
YX55
Nar_c
BT2
52
53
54
15.2
XL1
YX51
BT2
YX55
Wu26
55
56
16.1a
BT2
Wu23
57
58
16.1c
Wu23
BT2
57
58
16.2
Wu23
MSL
58
59
17.1a
Wu23
MSL
58
59
60
17.1c
Wu23
BT2
HOL16
MSL
58
59
60
17.2
Wu23
MSL
BT2
Wu26
Hol-16
Sant4
59
61
63
18
YX46
BT2
XY2
Sant4
BT5
Bt2
63
65
67
19.2
JFYK7
SB22
YX46
MSL
BTV3
70
72
74
20c
YX46
BTV3
SB22
Bt2
Nar-c
K1
Sant4
74
76
78
21.1e
WXSM51
Sant4
Bt2
82
84
86
88
22g
CC5
SB22
89
90
91
92
24.1a
SX7
D3
105
106
107
108
24.1c
SX29
SX7
D3
105
106
107
108
24.2
EXC3
Bt2
108
110
112
25c
SCH7
CC28
114
115
116
SIOC19 age
ASM age
SASM age
EM age
ASM records
SASM records
EM records

Fig. S6 The age-offset between the NGRIP GICC05/GICC05modelext chronology and the SIOC19 ages at the onset of interstadials. (A) The age difference (y-axis, in kyr) between the NGRIP GICC05 or GICC05modelext age and composite speleothem age (SIOC19) for each interstadial onset versus the age estimate of the event in NGRIP according to the GICC05 and GICC05modelext chronologies. Filled diamonds represent interstadial onsets for which speleothem data is available from multiple regions. Open circles represent interstadial onsets for which speleothem data is available from only a single region. Vertical error bars are 2σ age uncertainties from the SIOC19 ages. The dotted line (mostly out of frame) represents the mean counting error of the GICC05 chronology. For reference, the dashed lines represent an age offset of ±1%. (B) Robust regression line-of-best-fit between the GICC05 ages (up to 60 kyr BP) and SIOC19 ages for the synchronous interstadial onsets. The error ellipses represent the uncertainty in both the GICC05 chronology (i.e. Maximum Counting Error) and the composite speleothem estimates (see Table 1). The line-of-best-fit is defined by the function Age_{GICC05} = 1.000 * Age_{SIOC19} - 48 (-160 / +240) years. (C -F) The age offset between the ice-core and the composite speleothem ages plotted against (C) Northern Hemisphere Summer Insolation (NHSI) at 65°N *(81)*; (D) CO_2 concentration *(76)*; (E) interstadial abruptness (measured as the magnitude of change in NGRIP $\delta^{18}O$ divided by the duration of the transition); (F) interstadial onset amplitude (measured as the magnitude of change in NGRIP $\delta^{18}O$ across the transition). The same conclusions apply to the subset of data used to compare timing between both monsoon regions, and between the combined monsoon regions and Europe-Mediterranean (see Table S3 and the main text).

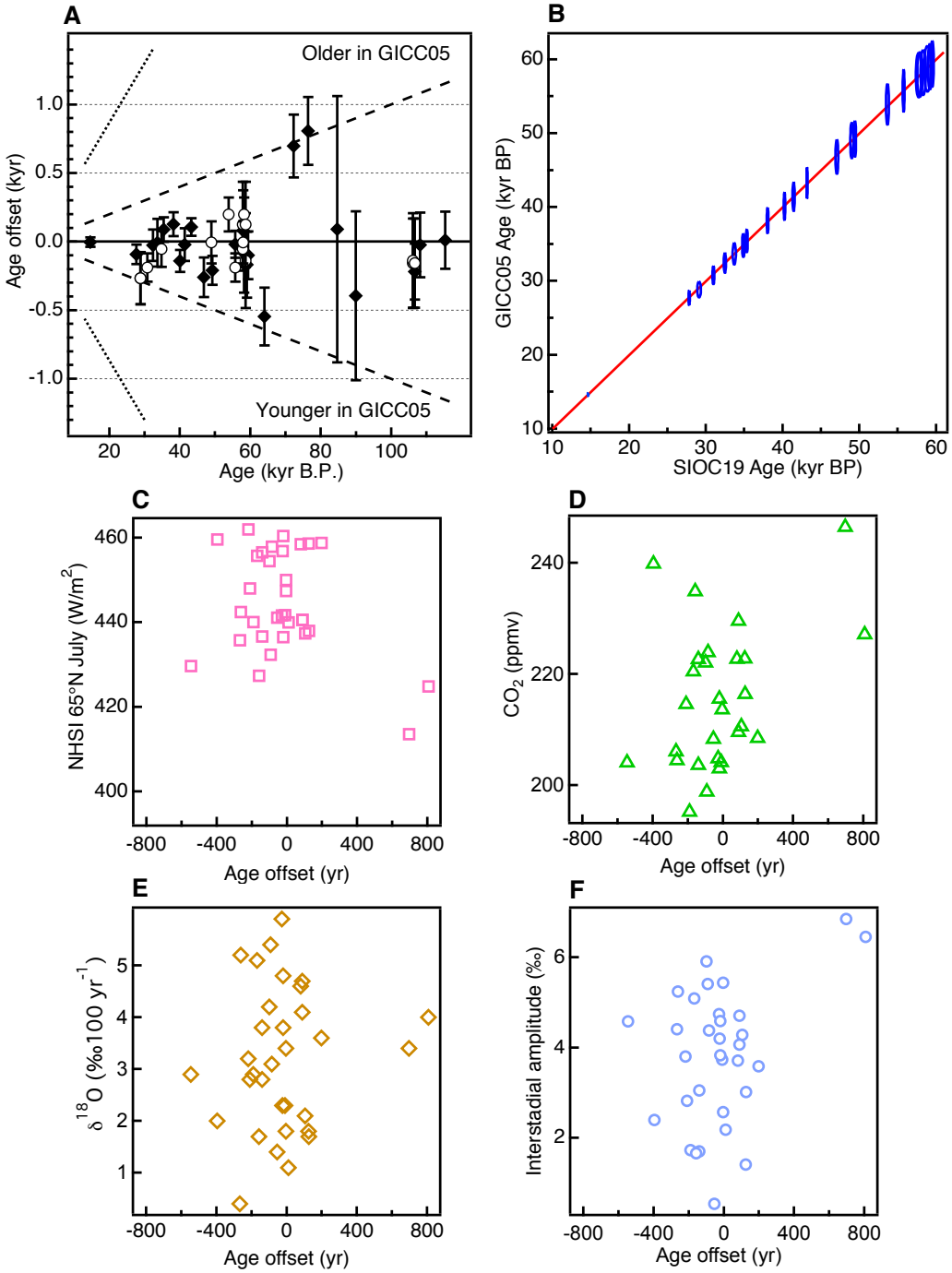
A
Older in GICC05
Younger in GICC05
Age offset (kyr)
Age (kyr B.P.)
B
GICC05 Age (kyr BP)
SIOC19 Age (kyr BP)
C
NHSI 65°N July (W/m^2)
Age offset (yr)
D
CO_2 (ppmv)
Age offset (yr)
E
$\delta^{18}O$ (‰100 yr^{-1})
Age offset (yr)
F
Interstadial amplitude (‰)
Age offset (yr)

Fig. S7. **Composite maps of (A) monthly mean precipitation anomalies and (B) monthly mean air temperature anomalies between simulated interstadial and stadial mean states for four modelling scenarios (see Methods)**. CO_2 composite (*20*), ICE (*19*), hosing composite (*19*, *20*), and these three combined. Units: (A) mm/month /10Sv (Sv=$10^6 m^3/s$), (B) °C /10Sv.

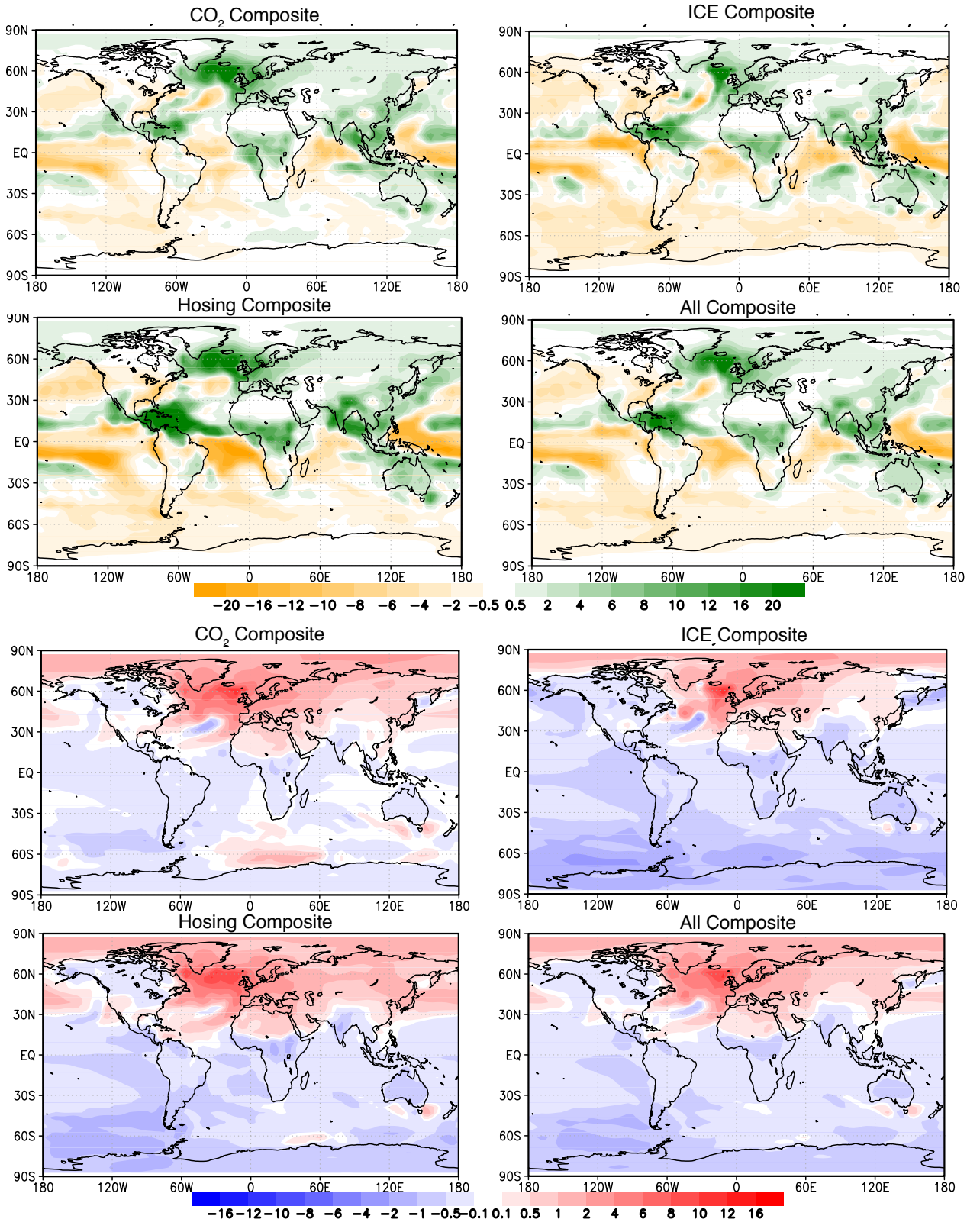
CO2 Composite
ICE Composite
Hosing Composite
All Composite
90N
60N
30N
EQ
30S
60S
90S
180
120W
60W
0
60E
120E
180
−20 −16 −12 −10 −8 −6 −4 −2 −0.5 0.5 2 4 6 8 10 12 16 20
CO2 Composite
ICE Composite
Hosing Composite
All Composite
−16 −12 −10 −8 −6 −4 −2 −1 −0.5 −0.1 0.1 0.5 1 2 4 6 8 10 12 16

Fig. S8. Examples where published depth-age models were modified following reprocessing of depth-age data for this study. These examples show cases where the reprocessing has led to sizeable changes in the chronology. Panels at left show the depth-age models from the original publication (blue) and from the finite-positive-growth-rate modelling undertaken in this study (red line gives mean depth-age relationship with 1σ (red shading) and 2σ (pink shading) uncertainty estimates). The original U-Th ages are in light blue and recalculated ages in black. The right-hand panels show the isotope records on their original (blue) and revised (red) age models compared to NGRIP *(2)* (black; plotted on the GICC05 chronology). Interstadial onset identification points are shown by black squares. (A) XL1 Xinglong Cave *(35)*. The original model was developed using StalAge *(62)*, which, in combination with slightly older original age calculations, has produced a different depth-age path. (B) Wu23 Wulu Cave *(78)*. Original age determinations were slightly older and revised modelling has forced the age model through a slightly younger path at the age determination at ~480 mm, reducing the growth rate below it. (C) St8 Santana Cave *(82)*. The age determination at 860 mm has been treated as an outlier and disregarded from the original (linear interpolation) model. This date did not meet the rejection criteria in our new depth-age model. The original approach gives a better fit to NGRIP but the revised model is used as this study requires that the derivation of age models be independent of their $\delta^{18}O$ records.

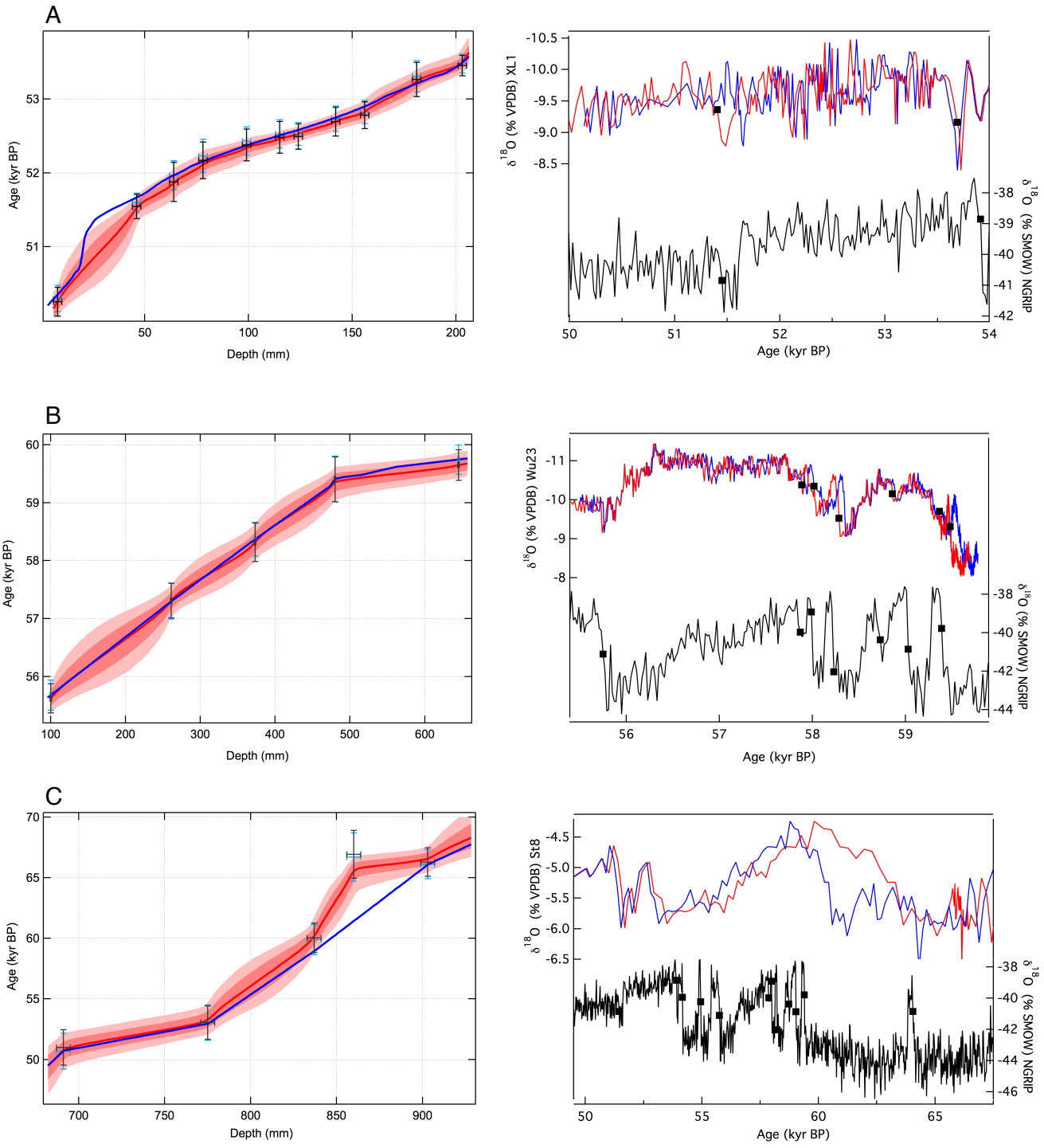
A
Age (kyr BP)
Depth (mm)
δ18O (% VPDB) XL1
δ18O (% SMOW) NGRIP
Age (kyr BP)
B
Age (kyr BP)
Depth (mm)
δ18O (% VPDB) Wu23
δ18O (% SMOW) NGRIP
Age (kyr BP)
C
Age (kyr BP)
Depth (mm)
δ18O (% VPDB) St8
δ18O (% SMOW) NGRIP
Age (kyr BP)

Table S1. List of speleothem records included in the compilation. Records are grouped by region (ASM: Asian Summer Monsoon, EM: Europe and Mediterranean, SAM: South American Monsoon) and are listed alphabetically by cave site.

Ref. number	Region	Cave	Sample Name	Country	Latitude	Longitude	Elevation (m a.s.l)	Min age (ka)	Max age (ka)	Reference
	ASM									
1		Bittoo	BT1 BT2 BT5	India	30.790	77.776	3000	11.7 70.95 27.97	25.33 24.86 144.9	Kathayat, G. *et al.* Indian monsoon variability on millennial-orbital timescales. *Scientific Reports* 6, 24374–7 (2016).
2		Dashibao	DSB3	China	26.083	105.050	1106	26.15	32.67	Zhao, K., Wang, Y., Edwards, R. L., Cheng, H. & Liu, D. High-resolution stalagmite δ18O records of Asian monsoon changes in central and southern China spanning the MIS 3/2 transition. *Earth and Planetary Science Letters* 298, 191–198 (2010).
3		Dongge	D4	China	25.283	108.083	680	9.97	15.79	Yuan, D. Timing, Duration, and Transitions of the Last Interglacial Asian Monsoon. *Science* 304, 575–578 (2004). Dykoski, C. et al. A high-resolution, absolute-dated Holocene and deglacial Asian monsoon record from Dongge Cave, China. Earth and Planetary Science Letters 233, 71–86 (2005).
			D3					99.04	125.64	Yuan, D. Timing, Duration, and Transitions of the Last Interglacial Asian Monsoon. Science 304, 575–578 (2004). Kelly, M. J. et al. High resolution characterization of the Asian Monsoon between 146,000 and 99,000 years B.P. from Dongge Cave, China and global correlation of events surrounding Termination II. Palaeogeography, Palaeoclimatology, Palaeoecology 236, 20–38 (2006).
4		Furong	FR5	China	29.217	107.900	480	7.65	15.51	Li, T.-Y. *et al.* Oxygen and carbon isotopic systematics of aragonite speleothems and water in Furong Cave, Chongqing, China. *Geochimica et Cosmochimica Acta* 75, 4140–4156 (2011).
5		Hulu	H82	China	32.058	119.045		12.09	16.16	Yuan, D. Timing, Duration, and Transitions of the Last Interglacial Asian Monsoon. *Science* 304, 575–578 (2004). Wu, J., Wang, Y., Cheng, H. & Edwards, R. L. An exceptionally strengthened East Asian summer monsoon event between 19.9 and 17.1 ka BP recorded in a Hulu stalagmite. SCI CHINA SER D 52, 360–368 (2009).
			MSL MSD PD					35.86 18.21 10.61	56.57 53.18 19.30	Wang *et al.* A High-Resolution Absolute-Dated Late Pleistocene Monsoon Record from Hulu Cave, China. *Science* 294, 2345–2348 (2001).
6		Jintanwan	J1	China	29.483	109.533	460	14.35	29.56	Cosford, J. *et al.* The East Asian monsoon during MIS 2 expressed in a speleothem δ18O record from Jintanwan Cave, Hunan, China. *Quaternary Research* 73, 541–549 (2010).
7		Maboroshi	Hiro-1	Japan	34.817	133.217	450	12.61	15.53	Shen, C.-C. *et al.* East Asian monsoon evolution and reconciliation of climate records from Japan and Greenland during the last deglaciation. *Quaternary Science Reviews* 29, 3327–3335 (2010).
8		Mawmluh	MWS-1	India	25.262	91.882	1290	5.30	33.53	Dutt, S. *et al.* Abrupt changes in Indian summer monsoon strength during 33,800 to 5500 years B.P. *Geophys. Res. Lett.* 42, 5526–5532 (2015).
9		Moomi	M1-5	Yemen	12.500	54.000	400	11.06	27.03	Shakun, J. D. *et al.* A high-resolution, absolute-dated deglacial speleothem record of Indian Ocean climate from Socotra Island, Yemen. *Earth and Planetary Science Letters* 259, 442–456 (2007).
10		Sanbao	SB22 SB25	China	31.667	110.433	1902	55.44 78.03	94.85 94.89	Wang, Y. et al. Millennial- and orbital-scale changes in the East Asian monsoon over the past 224,000 years. Nature 451, 1090–1093 (2008). Xia, Z., Kong, X., Jiang, X. & Cheng, H. Precise dating of East-Asian-Monsoon D/O events during 95–56 ka BP: Based on stalagmite data from Shanbao Cave at Shennongjia, China. SCI CHINA SER D 50, 228–235 (2007).
			SB23					98.54	130.75	Wang, Y. et al. Millennial- and orbital-scale changes in the East Asian monsoon over the past 224,000 years. Nature 451, 1090–1093 (2008).
			SB46					26.58	32.23	Zhao, K., Wang, Y., Edwards, R. L., Cheng, H. & Liu, D. High-resolution stalagmite δ18O records of Asian monsoon changes in central and southern China spanning the MIS 3/2 transition. *Earth and Planetary Science Letters* 298, 191–198 (2010).
11		Sanxing	SX7 SX29	China	27.367	107.183	720	86.49 106.02	108.39 109.22	Jiang, X. *et al.* Stalagmite-inferred abrupt climate change of Asian Summer Monsoon at MIS 5a/4 transition. *Climate of the Past Discussions* 1–22 (2017).
12		Shizi	SI3	China	32.400	107.167	680	46.37	53.29	Zhou, H., Zhao, J., Qing, W., Feng, Y.-X. & Tang, J. Speleothem-derived Asian summer monsoon variations in Central China, 54-46 ka. *J. Quaternary Sci.* 26, 781–790 (2011).
13		Songjia	SJ1	China	32.413	107.179	680	13.69	42.93	Zhou, H. *et al.* Heinrich event 4 and Dansgaard/Oeschger events 5–10 recorded by high-resolution speleothem oxygen isotope data from central China. *Quaternary Research* 82, 394–404 (2014).
			SJ3					9.06	19.78	Zhou, H. *et al.* Distinct climate change synchronous with Heinrich event one, recorded by stable oxygen and carbon isotopic compositions in stalagmites from China. *Quaternary Research* 69, 306–315 (2008).
14		Suozi	SZ2	China	32.433	107.167		102.43	119.14	Zhou, H. *et al.* Decoupling of stalagmite-derived Asian summer monsoon records from North Atlantic

										temperature change during marine oxygen isotope stage 5d. *Quaternary Research* 70, 315–321 (2008).
15		Wanxiang	WXSM51	China	33.317	105.000	1194	78.78	90.73	Johnson, K. R., Lynn Ingram, B., Sharp, W. D. & Zhang, P. East Asian summer monsoon variability during Marine Isotope Stage 5 based on speleothem δ18O records from Wanxiang Cave, central China. *Palaeogeography, Palaeoclimatology, Palaeoecology* 236, 5–19 (2006).
16		Wulu	Wu3	China	26.050	105.083	1440	28.63	39.16	Duan, W.-H. *et al.* A high-resolution monsoon record of millennial-scale oscillations during Late MIS 3 from Wulu Cave, south-west China. *J. Quaternary Sci.* 29, 83–90 (2014).
			Wu23					55.26	59.70	Liu, D. *et al.* Sub-millennial variability of Asian monsoon intensity during the early MIS 3 and its analogue to the ice age terminations. *Quaternary Science Reviews* 29, 1107–1115 (2010). Liu, D. et al. Strong coupling of centennial-scale changes of Asian monsoon and soil processes derived from stalagmite d18O and d13C records, southern China. Quaternary Research 85, 333–346 (2016).
			Wu26					58.27	61.16	Liu, D. *et al.* Sub-millennial variability of Asian monsoon intensity during the early MIS 3 and its analogue to the ice age terminations. *Quaternary Science Reviews* 29, 1107–1115 (2010).
			Wu32					20.78	29.02	Zhao, K., Wang, Y., Edwards, R. L., Cheng, H. & Liu, D. High-resolution stalagmite δ18O records of Asian monsoon changes in central and southern China spanning the MIS 3/2 transition. *Earth and Planetary Science Letters* 298, 191–198 (2010).
17		Xiangshui	X3	China	25.250	110.917	380	18.95	49.74	Cosford, J. *et al.* Millennial-scale variability in the Asian monsoon: Evidence from oxygen isotope records from stalagmites in southeastern China. *Palaeogeography, Palaeoclimatology, Palaeoecology* 266, 3–12 (2008).
18		Xiaobailong	XBL-1	China	24.200	110.917	1500	36.02	52.57	Cai, Y. *et al.* High-resolution absolute-dated Indian Monsoon record between 53 and 36 ka from Xiaobailong Cave, southwestern China. *Geol* 34, 621–5 (2006).
19		Xinglong	XL-1	China	40.483	117.483	710	49.92	56.73	Duan, W.-H., Cheng, H., Tan, M. & Edwards, R. L. Onset and duration of transitions into Greenland Interstadials 15.2 and 14 in northern China constrained by an annually laminated stalagmite. *Sci Rep* 6, 20844–6 (2016).
20		Xinya	XY2	China	30.583	109.467		60.07	69.55	Li, T.-Y. *et al.* High-resolution climate variability of southwest China during 57–70 ka reflected in a stalagmite δ 18O record from Xinya Cave. *SCI CHINA SER D* 50, 1202–1208 (2007).
21		Yamen	Y1	China	25.483	107.900		7.20	15.86	Yang, Y. *et al.* Precise dating of abrupt shifts in the Asian Monsoon during the last deglaciation based on stalagmite data from Yamen Cave, Guizhou Province, China. *Sci. China Earth Sci.* 53, 633–641 (2010).
22		Yangkou	JFYK7	China	29.020	107.183	2140	48.65	75.37	Han, L.-Y. *et al.* Potential influence of temperature changes in the Southern Hemisphere on the evolution of the Asian summer monsoon during the last glacial period. *Quaternary International* 392, 239–250 (2016).
23		Yaoba Don	YB1	China	28.800	109.833	420	8.84	29.84	Cosford, J. *et al.* Millennial-scale variability in the Asian monsoon: Evidence from oxygen isotope records from stalagmites in southeastern China. *Palaeogeography, Palaeoclimatology, Palaeoecology* 266, 3–12 (2008).
24		Yongxing	YX46 YX51 YX55	China	31.583	111.233		61.17 22.03 34.74	89.01 57.38 65.36	Chen, S. *et al.* Strong coupling of Asian Monsoon and Antarctic climates on sub- orbital timescales. *Sci Rep* 1–8 (2016). doi:10.1038/srep32995
	EM									
25		Beatus	EXC3 EXC4	Switzerland	46.633	7.817	875	101.19 77.15	110.22 107.12	Boch, R. *et al.* NALPS: a precisely dated European climate record 120–60 ka. *Clim. Past* 7, 1247–1259 (2011).
26		Corchia	CC5	Italy	44.033	10.283	840	89.27	128.69	Drysdale, R. N. Stalagmite evidence for the onset of the Last Interglacial in southern Europe at 129 ± 1 ka. *Geophys. Res. Lett.* 32, 1–4 (2005).
			CC28					95.44	118.37	Drysdale, R. N. *et al.* Stalagmite evidence for the precise timing of North Atlantic cold events during the early last glacial. *Geol* 35, 77–4 (2007).
27		Hölloch	Höl-7	Germany	47.133	10.250	1240–1438	46.65	48.75	Moseley, G. E. *et al.* Multi-speleothem record reveals tightly coupled climate between central Europe and Greenland during Marine Isotope Stage 3. *Geol* 42, 1043–1046 (2014).
			Höl-16					50.68	64.18	
28		Jeita	J2	Lebanon	33.950	35.650	100	13.15	20.43	Cheng, H. *et al.* The climate variability in northern Levant over the past 20,000 years. *Geophys. Res. Lett.* 42, 8641–8650 (2015).
29		Karaca	K1	Turkey	40.544	39.403	1536	5.82	104.80	Rowe, P. J. *et al.* Speleothem isotopic evidence of winter rainfall variability in northeast Turkey between 77 and 6 ka. *Quaternary Science Reviews* 45, 60–72 (2012).
30		Kleegruben	SPA 49	Austria	47.088	11.672	2165	48.59	58.21	Spötl, C. & Mangini, A. Stalagmite from the Austrian Alps reveals Dansgaard-Oeschger events during isotope stage 3:. Implications for the absolute chronology of Greenland ice cores. *Earth and Planetary Science Letters* **203,** 507–518 (2002).

			SPA 126					48.16	55.80	Spötl, C. & Mangini, A. Stalagmite from the Austrian Alps reveals Dansgaard-Oeschger events during isotope stage 3:. Implications for the absolute chronology of Greenland ice cores. Earth and Planetary Science Letters 203, 507–518 (2002).Spötl, C., Mangini, A. & Richards, D. A. Chronology and paleoenvironment of Marine Isotope Stage 3 from two high-elevation speleothems, Austrian Alps. Quaternary Science Reviews 25, 1127–1136 (2006).
31		Pindal	CAN	Spain	43.383	-3.500	24	18.10	25.68	Moreno, A. *et al.* A speleothem record of glacial (25–11.6kyr BP) rapid climatic changes from northern Iberian Peninsula. *Global and Planetary Change* 71, 218–231 (2010).
32		Schneckenloch	SCH7	Austria	47.433	9.867	1270	110.98	118.02	Boch, R. *et al.* NALPS: a precisely dated European climate record 120–60 ka. *Clim. Past* 7, 1247–1259 (2011).
33		Sieben Hengste	7H-2	Switzerland	46.770	7.830	1540	20.53	29.92	Luetscher, M. *et al.* North Atlantic storm track changes during the Last Glacial Maximum recorded by Alpine speleothems. *Nature Communications* 6, 1–6 (2015)
34		Sofular	So1	Turkey	41.417	31.933		24.10	51.02	Fleitmann, D. *et al.* Timing and climatic impact of Greenland interstadials recorded in stalagmites from northern Turkey. *Geophys. Res. Lett.* 36, L19707–5 (2009).
			So2					36.24	59.46	
	SAM									
35		Botuverá	BTV3A	Brazil	-26.777	-48.844	230	0	89.93	Wang, X. *et al.* Millennial-scale precipitation changes in southern Brazil over the past 90,000 years. *Geophys. Res. Lett.* 34, (2007).
			Bt2					0	115.55	Cruz, F. W., Jr. *et al.* A stalagmite record of changes in atmospheric circulation and soil processes in the Brazilian subtropics during the Late Pleistocene. *Quaternary Science Reviews* 25, 2749–2761 (2006). Cruz, F. W., Jr. et al. Insolation-driven changes in atmospheric circulation over the past 116,000 years in subtropical Brazil. Nature 434, 63–66 (2005).
36		Diamante	Nar-C	Peru	-4.267	-76.500	960	2.33	175.06	Cheng, H. *et al.* Climate change patterns in Amazonia and biodiversity. Nat Commun 4:1411. *Nature Communications* 4, 1411–6 (2013).
37		El Condor	ELC-B	Peru	-4.067	-76.700	860	4.30	53.37	Cheng, H. *et al.* Climate change patterns in Amazonia and biodiversity. Nat Commun 4:1411. *Nature Communications* 4, 1411–6 (2013).
38		Pacupahuain	P09PH2	Peru	-11.240	-75.820	3800	15.92	49.74	Kanner, L. C., Burns, S. J., Cheng, H. & Edwards, R. L. High-Latitude Forcing of the South American Summer Monsoon During the Last Glacial. *Science* 335, 570–573 (2012).
39		Santana	St8	Brazil	-23.469	-47.273	550	0	131.78	Cruz, F. W., Jr., Burns, S. J., Karmann, I., Sharp, W. D. & Vuille, M. Reconstruction of regional atmospheric circulation features during the late Pleistocene in subtropical Brazil from oxygen isotope composition of speleothems. *Earth and Planetary Science Letters* 248, 495–507 (2006).
40		Santiago	Sant4 Sant5	Ecuador	-2.983	-77.867	980	35.20 34.63	93.58 46.39	Mosblech, N. A. S. *et al.* North Atlantic forcing of Amazonian precipitation during the last ice age. *Nature Geoscience* 5, 817–820 (2012).

Table S2. Summary of the timing of interstadial onsets based on the compilation of multiple speleothem records. MSWD, Mean Square Weighted Deviation. Regional speleothem ages are error-weighted means based on multiple individual speleothem records within a given region (*n* denotes the number of records). The combined speleothem age (SIOC19) and uncertainty is the error-weighted mean of the regional ages. Total other records includes all records that met the criteria for event identification (resolution of at least three data points per thousand year, chronological precision better than 3.5%) and cover the time interval for the event (Fig. S3), but in which the event has not been identified. In the majority of cases the resolution was insufficient to detected the event; see for example, many of the short-lived events around interstadial 16 and 17 which require decadal or sub-decadal resolution in order to be resolved. Section A presents the timing of interstadial events for which synchronous timing can be demonstrated across multiple regions. Section B presents event ages using speleothem records from only one region because other regions lack high-quality records. Section C presents the regional ages for the two non-synchronous events. Section D presents the three unresolved events. All other interstadials not listed were not detected in at least two speleothem records. The corresponding GICC05 / GICC05modelext age and uncertainty for each event is shown *(3)*. Errors are not provided beyond the limits of annual layer counting (60 kyr BP). All age errors shown are ±2σ uncertainties, and all ages are reported as kyr BP (before 1950).

	Interstadial number	Europe-Mediterranean Age	2s	n	Asian Summer Monsoon Age	2s	n	South American Monsoon Age	2s	n	Other total records	Combined speleothem SIOC19 Age	2s	n	MSWD	GICC05 / GICC05modelext Age	MCE
A	1e	14,421 ±	343	1	14,648 ±	34	7(1)	14,733 ±	323	1	0	14,646 ±	34	9	1.01	14,642 ±	186
	3	27,822 ±	127	2	27,825 ±	90	5	27,789 ±	330	3	4	27,822 ±	72	10	0.02	27,730 ±	832
	5.1	31,099 ±	266	1	31,000 ±	230	3	30,946 ±	127	3	3	30,980 ±	103	7	0.55	30,790 ±	1,024
	5.2	32,561 ±	155	1	32,379 ±	296	3	32,367 ±	214	3	1	32,477 ±	115	7	1.34	32,450 ±	1,132
	6	33,770 ±	282	1	33,611 ±	457	1	33,668 ±	252	3	4	33,699 ±	174	5	0.23	33,690 ±	1,212
	7a	35,103 ±	516	1				34,869 ±	135	2	5	34,884 ±	130	3	0.77	34,830 ±	1,293
	7c	35,712 ±	455	1	35,359 ±	123	2	35,287 ±	139	3	3	35,342 ±	90	6	1.68	35,430 ±	1,321
	8c	38,057 ±	127	2	38,025 ±	130	7	38,094 ±	380	2	3	38,044 ±	88	11	0.10	38,170 ±	1,449
	9	40,235 ±	199	2	40,253 ±	89	3	40,210 ±	763	1	5	40,251 ±	81	8	0.02	40,110 ±	1,580
	10	41,602 ±	242	2	41,355 ±	155	6	41,455 ±	291	2	1	41,431 ±	119	10	1.48	41,410 ±	1,633
	11	43,556 ±	517	1	43,181 ±	65	5	43,093 ±	483	1	4	43,185 ±	64	7	1.11	43,290 ±	1,736
	12c	46,975 ±	222	4	unresolved		7	47,141 ±	191	2	0	47,071 ±	145	6	1.28	46,810 ±	1,912
	13a	48,927 ±	492	1(1)	48,998 ±	192	3	49,091 ±	300	1	7	49,015 ±	154	5	0.21	49,010 ±	2,021
	13c	49,478 ±	135	4	49,378 ±	169	3				7	49,439 ±	106	7	0.85	49,230 ±	2,031
	14c	53,662 ±	253	1	53,740 ±	143	4	53,106 ±	1,090	1	7	53,713 ±	124	6	0.77	53,910 ±	2,289
	17.1c	59,236 ±	871	1	59,195 ±	251	3				10	59,199 ±	241	4	0.01	59,030 ±	2,557
	17.2	59,825 ±	664	1	59,455 ±	180	4(1)	60,421 ±	1,740	1	7	59,489 ±	173	6	1.16	59,390 ±	2,569
	18				64,576 ±	217	4	64,948 ±	914	2	6	64,596 ±	211	6	0.63	64,050	
	19.2				71,590 ±	232	4	71,891 ±	1,949	1	2	71,594 ±	230	5	0.09	72,290	
	20c	75,954 ±	1,718	1	75,574 ±	267	2	75,578 ±	740	4	0	75,583 ±	248	7	0.10	76,390	
	21.1e				85,097 ±	1,318	1	84,055 ±	1,437	2	3	84,621 ±	971	3	1.14	84,710	
	22g	90,573 ±	787	1	90,090 ±	992	1				4	90,386 ±	617	2	0.07	89,990	
	24.2	108,244 ±	235	1	unresolved		4	109,160 ±	2,249	1	1	108,254 ±	234	2	0.66	108,230	
B	4	unresolved		2	unresolved		6	29,117 ±	189	4	1	29,117 ±	189	4	1.15	28,850 ±	898
	15.2				55,770 ±	98	5				6	55,770 ±	98	5	2.00	55,750 ±	2,368
	16.1a				57,746 ±	311	2				11	57,746 ±	311	2	2.30	57,870 ±	2,492
	16.1c				57,910 ±	293	2				11	57,910 ±	293	2	1.29	57,990 ±	2,497
	16.2				58,315 ±	288	2				11	58,315 ±	288	2	0.37	58,230 ±	2,511
	17.1a				58,870 ±	346	2				12	58,870 ±	346	2	0.02	58,730 ±	2,540
	24.1a				106,328 ±	325	2				7	106,328 ±	325	2	0.25	106,170	
	24.1c				106,918 ±	204	3				6	106,918 ±	204	3	0.20	106,700	
	25c	115,310 ±	209	2							5	115,310 ±	209	2	0.97	115,320	
C	15.1	55,073 ±	128	2	54,739 ±	134	4				8				12.92	54.95 ±	2.338
	23.2	104,120 ±	165	2	104,836 ±	235	2				5				24.85	104.47	
D	12a				unresolved		4			1	8					44,510 ±	1,791
	14e	unresolved		3	unresolved		6			1	3					54,170 ±	2,310
	23.1	unresolved		3	unresolved		2				4					103,990	

Table S3. Age offset between regional speleothem estimates for interstadials. EM, Europe-Mediterranean; EWM, Error Weighted Mean; MSWD, Mean Square Weighted Deviation. (A) Interstadial ages for those events recorded in at least two records from the ASM and SAM and the age offset between both. (B) Interstadial ages for those events recorded in at least two records from the EM and Monsoon (either ASM and/or SAM) and offset ages between both. Numbers in brackets give the number of records for each region. Ages are given in kyr BP. All uncertainties are 2σ.

A

Interstadial	ASM		SAM		Offset (ASM-SAM)	
3	27.825 ± 0.090	(5)	27.789 ± 0.330	(3)	0.037 ±	0.342
5.1	31.000 ± 0.230	(3)	30.946 ± 0.127	(3)	0.054 ±	0.263
5.2	32.379 ± 0.296	(3)	32.367 ± 0.214	(3)	0.012 ±	0.366
7c	35.359 ± 0.123	(2)	35.287 ± 0.139	(3)	0.072 ±	0.186
8c	38.025 ± 0.130	(7)	38.094 ± 0.380	(2)	-0.070 ±	0.401
10	41.355 ± 0.155	(6)	41.455 ± 0.291	(2)	-0.100 ±	0.329
18	64.576 ± 0.217	(4)	64.948 ± 0.914	(2)	-0.372 ±	0.940
20c	75.574 ± 0.267	(2)	75.578 ± 0.740	(4)	-0.004 ±	0.786
				EWM	**0.019 ±**	**0.113**
				MSWD	0.26	

B

Interstadial	EM		Monsoon		Offset (EM-Monsoon)	
3	27.822 ± 0.127	(2)	27.823 ± 0.087	(8)	-0.001 ±	0.154
8c	38.057 ± 0.127	(2)	38.032 ± 0.123	(9)	0.026 ±	0.176
9	40.235 ± 0.199	(2)	40.254 ± 0.089	(4)	-0.018 ±	0.218
10	41.602 ± 0.242	(2)	41.377 ± 0.137	(8)	0.224 ±	0.278
12c	46.975 ± 0.222	(4)	47.141 ± 0.191	(2)	-0.166 ±	0.293
13c	49.478 ± 0.135	(4)	49.378 ± 0.169	(3)	0.100 ±	0.216
				EWM	**0.025 ±**	**0.084**
				MSWD	0.9	

Table S4. The details of the experiments used for composite of DO climate changes. $\delta\varphi$ represents changes in the strength of the Atlantic Meridional Overturning Circulation (AMOC) modes in each set of experiments. In the hosing scenario, the average of the last 100 model years is used to represent the corresponding hosing states (i.e. weak AMOC mode), which is then compared with their control state to determine the AMOC changes. In the ICE scenario, each set of experiments includes two equilibrium ocean states as described in ref. 16. That is, NHIS_0.4 represents experiments NHIS_0.4s NHIS_0.4w, NHIS_0.35 represents experiments NHIS_0.35s and NHIS_0.35w, and NHIS_0.3 represents experiments NHIS_0.3s and NHIS_0.3w.

	Experiment ID	Forcing details	Other boundary conditions	δφ	Reference
Hosing *					
	lgm015	0.15Sv freshwater flux into Ruddiman belt for 800 years	full LGM conditions	16.45	*(52)*
	lgm02	0.2Sv freshwater flux into Ruddiman belt for 1000 years	full LGM conditions	20.19	*(52)*
CO2					
	Hys_CO2	two AMOC states under a CO2 rang of 209 and 225ppm	20% LGM ice volume while the rest is identical to the LGM	12.017	*(20)*
	LGM_015_CO2	two AMOC states under a CO2 rang of 210 and 225 ppm	full LGM conditions with persistent 0.15Sv NA hosing	10.082	*(20)*
ICE					
	NHIS03	two AMOC states under 40% LGM ice volume	LGM conditions	8.61	*(19)*
	NHIS035	two AMOC states under 35% LGM ice volume	LGM conditions	8.004	*(19)*
	NHIS04	two AMOC states under 30% LGM ice volume	LGM conditions	7.598	*(19)*

*Reference state is the Last Glacial Maximum (LGM) control run, i.e. LGM-W in ref. 52.

Data S1. (separate file)

Individual speleothem event timings. This file provides the timing of the onset of interstadials in each of the individual speleothem records.

Data S2. (separate file)

Speleothem depth age models. This file provides the depth-age models produced for each of the speleothem data sets.

Data S3. (separate file)

Plots of the isotope records of speleothems used in the comparison. This file provides the full isotope record of all speleothem used in the comparison, grouped by region and showing all event identification points and sections of the records used.

Data S4. (separate file)

Code utilised for the calculation of uranium-thorium ages.

Data S5. (separate file)

The finite positive growth rate model source code for Wavemetrics Igor Pro.